Wake characteristics of a utility-scale wind turbine under coherent inflow structures and different operating conditions

Xiaolei Yang
Department of Civil Engineering, Department of Mechanical Engineering, College of Engineering and Applied Sciences, Stony Brook University, Stony Brook, New York 11794, USA

Fotis Sotiropoulos*
Department of Civil Engineering, College of Engineering and Applied Sciences, Stony Brook University, Stony Brook, New York 11794, USA

(Received 2 April 2018; published 12 February 2019)

Understanding the wake characteristics of wind turbines under the influence of atmospheric turbulence is crucial for developing advanced turbine control algorithms, such as the coordinated turbine control for improving the performance of the entire wind farm as an integrated system. In this work, we systematically investigate the wake of a utility-scale wind turbine for different thrust coefficients, which is relevant to the coordinated axial induction control. Large-eddy simulation (LES) with novel actuator surface models for turbine blades and nacelle is employed to simulate turbine wakes. Different thrust coefficients are achieved by varying the tip-speed ratio, i.e., $\lambda = 6.8, 7.8, 8.8, 9.3$. The inflow is generated from a precursory simulation using a very large computational domain to include the large-scale flow structures in atmospheric turbulence. The computed results show that varying the tip-speed ratio gives rise to differences in wake statistics, such as the wake recovery rate and the turbulence intensity. However, the computed results also reveal similarities in wakes from different tip-speed ratios. It is found that the characteristic velocity defined by the thrust on the rotor scales the turbine-added turbulence kinetic energy computed based on different wake center locations. For all considered tip-speed ratios, two dominant frequencies of the large-scale motion of the wake are observed, one is the dominant low frequency of the large-scale flow structures in the inflow prevailing at almost all downwind locations, the other one is the frequency of Strouhal number about 0.15 prevailing at far wake locations ($>3 \sim 4$ rotor diameters). The existence of the inflow frequency in the large-scale motion of wakes shows the effects of incoming large-scale flow structures on wake meandering. The Strouhal number of the second frequency, however, is typical for that of vortex shedding behind bluff bodies. This finding suggests the coexistence of the two mechanisms for wake meandering, i.e., inflow large-scale turbulent flow structures and the wake shear layer instability, with the corresponding motion termed inflow-driven wake meandering and shear-induced wake meandering, respectively. The effects of wake and turbine energy extraction on motion of different frequencies are examined for different tip-speed ratios. As approaching the turbine upwind, the energy of the low-frequency motion of the inflow is significantly attenuated, while the energy of the motion at frequencies higher than the inflow low frequency are observed to increase for most cases. In the near wake, decreases of energy are observed for all the frequencies in almost all the cases. At far wake locations, the energy of the motion at all frequencies is increased to a level higher than that of the inflow (at $2D$ turbine upwind) in almost all the cases. At last, the statistics of wake centers in the spanwise and vertical directions are

*Corresponding author: fotis.sotiropoulos@stonybrook.edu

examined. It is found that the probability density function (PDF) profiles of wake center fluctuations nearly collapse with each other for different tip-speed ratios. The Gaussian distribution is found to be an acceptable approximation for the PDF of wake center locations at near wake locations (e.g., $2D$, $4D$, and $6D$ turbine downwind), while it is a poor approximation at far wake locations (greater than $8D$ turbine downwind). Downwind variations of the mean values and the standard deviations of wake center fluctuations are also observed to nearly collapse with each other for different tip-speed ratios. The observed similarities of turbine wake statistics illuminate the possibility of developing advanced engineering models taking into account the unsteady features of turbine wakes for advanced turbine controls.

DOI: 10.1103/PhysRevFluids.4.024604

I. INTRODUCTION

The turbines in a wind farm are coupled with each other through turbine wakes and the interaction of turbine wakes with the atmospheric turbulence. The complexity of turbine wake dynamics in the atmospheric turbulent flow poses a great challenge for maximizing the performance of the entire wind farm as an integrated energy producing system using the advanced wind farm control strategies. There are several advanced wind farm control strategies existing in the literature, such as the coordinated turbine control through axial induction factor [1–3], the yaw-based and tilt-based wake redirection methods [3,4], and the individual pitch control (IPC)-based methods [4]. To develop such advanced turbine control algorithms requests an improved understanding of turbine wake dynamics and its interaction with the atmospheric turbulence for different turbine operating conditions. The particular interest of this work is to investigate the wake dynamics of a utility-scale wind turbine under an inflow with large-scale coherent structures for different tip-speed ratios, which is relevant to the coordinated axial induction control.

Inflow conditions have significant effects on turbine wake dynamics. Some studies focused on uniform inflows, e.g., Troldborg *et al.* [5] investigated the wake of a wind turbine operating in a uniform inflow at various tip-speed ratios. The uniform inflow case can provide insights into wake dynamics, e.g., tip and hub vortices and their interactions; however, it cannot represent the wind with shear and atmospheric turbulence in the real world. Investigations of turbine wakes under more realistic incoming wind conditions, which take into account the effects of different ground roughness, thermal stratifications, and terrain conditions, have been carried out in wind tunnel experiments [6]. For instance, Chamorro and Porté-Agel studied the wake of a model wind turbine placed on rough and smooth surfaces in Ref. [7], and the wake of the same model wind turbine under both neutral and stably stratified conditions in Ref. [8]. Zhang *et al.* [9] investigated the wake of a model wind turbine under convective boundary layer conditions. Investigations of turbine wakes under site-specific complex inflows were focused on simple terrain topography in wind tunnel experiments, e.g., Howard *et al.* [10] investigated the influences of the wake of a three-dimensional, sinusoidal hill on the wake of a model wind turbine. Chamorro *et al.* [11] investigated the effects of energetic coherent flow structures induced by upstream cylinders on the wake of an axial-flow hydrokinetic turbine. Wind tunnel experiments can provide valuable datasets for investigating the wake dynamics and validating computational models. However, the turbines employed in wind tunnel experiments are usually one to two orders of magnitude smaller than utility-scale wind turbines, which makes the findings of wind tunnel experiments not directly applicable to utility-scale wind turbines. Field-scale measurements [12–15] are very important for validating and verifying computational models and laboratory-scale experiments. However, the data obtained from field-scale measurements are usually constrained to certain locations and suffer from uncertainties from the environmental conditions and the turbine operating conditions. Compared with experiments in fields and laboratories, the advantage of high-fidelity computational models (e.g., LES) lies in their capability to provide high-resolution, three-dimensional wind fields in wakes

of utility-scale turbines under well-controlled inflow, terrain, and turbine operating conditions. The atmospheric realism of the inflow turbulent structures plays an important role on how well the LES predictions can represent the wake dynamics of utility-scale wind turbines in the real world. The synthetic turbulence technique is usually employed to generate the turbulence in the inflow; e.g., Yang *et al.* [16] investigated the effects of the synthetic turbulence on the LES of utility-scale wind turbines when using the wind field computed from the Weather Research and Forecasting (WRF) model as the inflow. Specific levels of turbulence intensity can be achieved using the synthetic turbulence technique. However, the generated large-scale flow structures are in general not realistic. More realistic turbulence in the inflow can be generated from a precursory simulation. Recently, a technique using spires at the inlet to generate energetic coherent structures in the inflow was developed by Foti *et al.* [17]. In the precursory simulation for inflows, the domain size of the precursory simulation is usually the same or comparable with that employed in the turbine simulation. The large-scale atmospheric turbulence can be captured in simulations of large wind farms because of the employed large computational domain. Such structures cannot be captured, however, in a small domain simulation of an individual turbine if the same domain size is employed in the precursory inflow simulation.

Nacelle-induced coherent structures were shown to have a significant impact on turbine wake characteristics, such as velocity deficits, turbulence intensities, and wake meandering [18–21]. It was shown in Ref. [22] that the actuator line model without a nacelle model cannot accurately capture the wake meandering of a hydrokinetic turbine, and it underpredicts the turbulence intensity at far wake locations. Santoni *et al.* [23] also found the effects of nacelle on the velocity deficits and turbulence intensity for the "Blind test 1" turbine at the Norwegian University of Science and Technology and proposed to use the immersed boundary method for modeling the turbine nacelle [24]. The nacelle can be represented by a permeable disk with a specified drag coefficient, which, however, cannot take into account the nacelle effect accurately as shown in Refs. [16,25]. In Ref. [25] an actuator surface model for nacelle was proposed, which can capture the nacelle wake dynamics and its effect on far wake meandering on coarse meshes typical to those used in actuator disk/line simulations. In this work, we employ LES with the actuator surface models for turbine blades and nacelle [25] for simulating the turbine wakes.

The objective of this work is to contribute toward the development of physics-based engineering wake models by advancing fundamental understandings of the wake dynamics of a utility-scale wind turbine under realistic inflow with large-scale turbulent flow structures. Turbine-added turbulence increases the dynamic loads on the downwind turbines. Yang *et al.* [26] found that the velocity defined by the thrust on the rotor ($U_T = \sqrt{T/\pi R^2}$, where T is the time-averaged thrust exerted on the turbine rotor, and R is the rotor radius) can serve as the proper velocity scale for the turbine-added turbulence kinetic energy (TKE) of the wake of a turbine located at different downwind locations from a three-dimensional hill. It was found in Ref. [27] that U_T can properly scale the turbine-added TKE for wakes from turbines of different designs. In the present work, we further examine the velocity U_T for scaling the turbine-added TKE computed based on wake center locations for a turbine operating with different tip speed ratios under the inflow with large-scale turbulent flow structures. Meandering describes the low-frequency, large-scale, bodily movement of turbine wakes. Two mechanisms exist in the literature for the origin of wake meandering. In one mechanism, it is hypothesized that the meandering is caused by the incoming large-scale turbulent flow structures, which advect wakes as passive scalars. In the other mechanism, the wake meandering is considered to be the result of the wake shear layer instability similar to that for the vortex shedding behind bluff bodies. The first mechanism forms the basis of the dynamic wake meandering model [28]. It was shown in Ref. [29] that the predictions from the dynamic wake meandering model are in good agreement with the field measurements. The second mechanism, however, is also supported by wind tunnel experiments [30,31], numerical simulations [22], and instability analysis [18]. In particular, meandering frequencies typical for the vortex shedding of bluff bodies were observed in Ref. [32] for different turbine operational regimes and in Ref. [27] for different turbine designs ranging from a model wind turbine of diameter 0.13 m to a utility-scale wind turbine of diameter 96

m. In the present work, we numerically examine the effects of the two mechanisms for a utility-scale turbine under inflows with large-scale turbulent flow structures. To include large-scale structures in the inflow, we generate the inflow from a precursory simulation using a very large computational domain and run the simulations sufficiently long to cover the low-frequency motion of the inflow (although it is still not long enough to ensure an uniformly distributed inflow in the spanwise direction, which will be discussed in Sec. IV), which is different from our previous work on the simulation of the same turbine [27]. At last we study the probability density function (PDF) of wake center locations for the simulated cases to examine whether the Gaussian distribution can model the PDF of wake center locations for the simulated cases.

The paper is organized as follows: the following section briefly describes the employed numerical methods including the flow solver and the actuator surface models for turbine blades and nacelle; the Sec. III describes the computational setup for both turbine simulations and inflow generation; the Sec. IV presents the computational results; and the Sec. V draws the conclusions of this paper.

II. NUMERICAL METHODS

The Virtual Flow Simulator (VFS-Wind) [16,25,33,34] code is employed for simulating the flow past the EOLOS turbine. VFS-Wind has been systematically validated using wind tunnel and field experiments. Recently, it was successfully applied to a utility-scale wind farm in complex terrain [35]. The governing equations are the three-dimensional, unsteady, filtered continuity and Navier-Stokes equations:

$$\frac{\partial u_i}{\partial x_i} = 0, \tag{1}$$

$$\frac{\partial u_i}{\partial t} + \frac{\partial u_i u_j}{\partial x_j} = -\frac{\partial p}{\partial x_i} + \frac{\partial}{\partial x_j}\left(\nu \frac{\partial u_i}{\partial x_j} - \tau_{ij}\right) + f_i, \tag{2}$$

where x_i are the Cartesian coordinates, u_i is the ith component of the velocity vector in Cartesian coordinates, ν is the kinematic viscosity, p is the pressure, f_i are the body forces introduced by the turbine blade and nacelle computed using the actuator surface models, and τ_{ij} represents the anisotropic part of the subgrid-scale stress tensor, which is modeled by the dynamic eddy viscosity subgrid-scale stress model [36]. The governing equations are discretized in space using a second-order accurate central differencing scheme, and integrated in time using the fractional step method [37]. An algebraic multigrid acceleration along with a GMRES solver is used to solve the pressure Poisson equation. A matrix-free Newton-Krylov method is used for solving the discretized momentum equations.

We briefly describe the actuator surface models for blades and nacelle, respectively. In the actuator surface models, we have two sets of independent meshes, i.e., the background Cartesian grid for the flow with its coordinate denoted by $\mathbf{x}$ (x, y, z or x_1, x_2, x_3), and the Lagrangian grid following the actuator surfaces with its coordinate denoted by $\mathbf{X}$ (X, Y, Z or X_1, X_2, X_3). In the actuator surface model for the rotor blades, the actuator surface is formed by airfoil chords at different radial locations. In the actuator surface model for nacelle, the actuator surface is the actual surface of the nacelle. The effects of the blade and nacelle surfaces on the incoming wind are represented by distributed body forces. In general, the grid nodes on the actuator surfaces do not coincide with the background fluid nodes. The smoothed discrete delta function developed in Ref. [38] is employed for spreading the forces from the actuator surfaces to the background grids as follows:

$$f_i(\mathbf{x}) = -\sum_{\mathbf{X}\in g_{\mathbf{X}}} f_i(\mathbf{X})\delta_h(\mathbf{x}-\mathbf{X})A(\mathbf{X}), \tag{3}$$

where $f_i(\mathbf{X})$ are the forces the air exerts on the turbine structure, and A is the area of the surface mesh element. The major difference between the actuator surface models for blades and nacelle is

how the forces on the actuator surfaces are computed. In the actuator surface model for blade, the forces are computed using the blade element method as follows:

$$\mathbf{L} = \tfrac{1}{2}\rho C_L c|\mathbf{V}_{\text{rel}}|^2\mathbf{e}_L \tag{4}$$

and

$$\mathbf{D} = \tfrac{1}{2}\rho C_D c|\mathbf{V}_{\text{rel}}|^2\mathbf{e}_D, \tag{5}$$

where C_L and C_D are the lift and drag coefficients, $\mathbf{e}_L$ and $\mathbf{e}_D$ are the unit vectors for the directions of lift and drag. To account for the three-dimensional rotational effect and ensure physical behavior of forces near the tip, the stall delay model developed by Du and Selig [39] and the tip-loss correction proposed by Shen *et al.* [40,41] are employed to correct the lift and drag coefficients, respectively. The relative incoming velocity $\mathbf{V}_{\text{rel}}$ employe in Eqs. (4) and (5) is computed by

$$\mathbf{V}_{\text{rel}} = u_x\mathbf{e}_x + (u_\theta - \Omega r)\mathbf{e}_\theta \tag{6}$$

at each radial location, where Ω is the rotational speed of the rotor, and $\mathbf{e}_x$ and $\mathbf{e}_\theta$ are the unit vectors in the axial and azimuthal directions, respectively. The u_x and u_θ are the axial and azimuthal components of the flow velocity interpolated from the background grid nodes and averaged over the chord for each radial locations. The computed lift and drag forces are then uniformly distributed in the chordwise direction at each radial location. In the actuator surface model for nacelle, the force in the surface normal direction is computed by satisfying the nonpenetration condition as in the direct forcing immersed boundary method, which can be expressed as follows:

$$\mathbf{f}_n(\mathbf{X}) = \frac{h[-\mathbf{u}^d(\mathbf{X}) + \tilde{\mathbf{u}}(\mathbf{X})]\cdot\mathbf{e}_n(\mathbf{X})}{\Delta t}\mathbf{e}_n(\mathbf{X}), \tag{7}$$

where $\mathbf{u}^d(\mathbf{X})$ is the desired velocity on the nacelle surface, $\mathbf{e}_n(\mathbf{X})$ is the unit vector in the normal direction of the nacelle surface, $h = (h_x h_y h_z)^{1/3}$ is the length scale of the local background grid spacing, $\tilde{\mathbf{u}}(\mathbf{X})$ is the estimated velocity on the actuator surface interpolated from the background grid nodes. The tangential force acting on the surface per unit area is computed as

$$\mathbf{f}_\tau(\mathbf{X}) = \tfrac{1}{2}c_f U^2\mathbf{e}_\tau(\mathbf{X}), \tag{8}$$

where c_f is calculated from the empirical relation proposed by Schultz-Grunow [42] for turbulent boundary layers with zero pressure gradient, i.e., $c_f = 0.37(\log \text{Re}_x)^{-2.584}$, where Re_x is the Reynolds number based on the incoming velocity and the distance from the upstream edge of the immersed body, and U is the local mean incoming velocity (in the present cases, it is the mean downwind velocity upwind of the turbine at turbine hub height). For details of the actuator surface models for blades and nacelle, the reader is referred to Ref. [25].

III. COMPUTATIONAL SETUP

The three-bladed Clipper Liberty 2.5 MW research wind turbine operated by the EOLOS Wind Energy Research Consortium at the University of Minnesota is employed. Several experimental [43–45] and computational studies [27,46,47] have been carried out using this turbine. The power and thrust coefficients of the EOLOS turbine can be changed by adjusting the blade pitch and the tip-speed ratio (the tip-speed ratio is defined as $\lambda = \frac{\Omega R}{U_h}$, where Ω is the rotor rotational speed, R is the rotor radius, and U_h in the incoming wind speed at hub height). In this work, we focus on the so-called region 2, in which the blade pitch remains constant and thus we will vary the tip-speed ratio to obtain different thrust coefficients. The diameter of the turbine is $D = 96$ m. The hub height of the turbine is $z_h = 80$ m. The computational domain size is $L_x \times L_y \times L_z = 22D \times 10D \times 10D$ with the number of grids nodes $N_x \times N_y \times N_z = 433 \times 339 \times 152$ in the downwind (x), spanwise (y), and vertical (z) directions, respectively. The wind turbine is located at $x = 0$ and $y = 0$ location. The ground is located at $z = 0$. In the wind turbine and near wake region, the grid spacings are $\Delta x = \Delta y = \Delta z = D/48$. The height of the computational domain represents the thickness of atmospheric

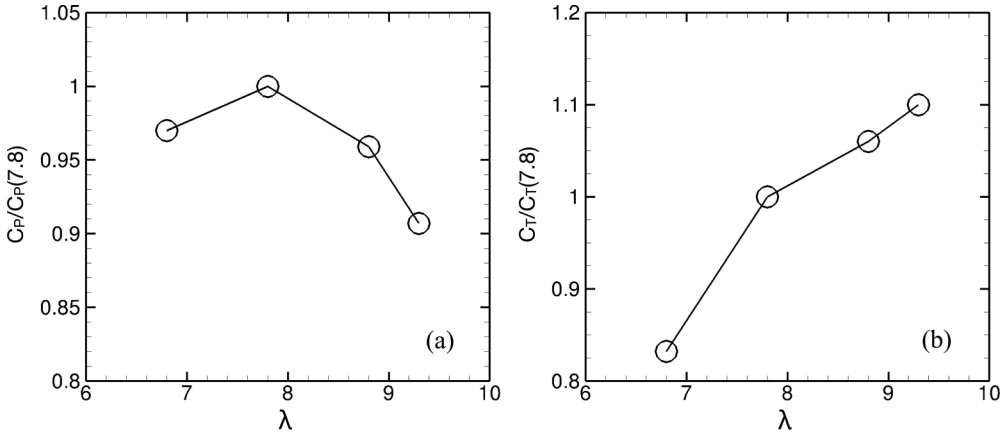

FIG. 1. Power (a) and thrust (b) coefficients for different tip-speed ratios of the EOLOS wind turbine.

boundary layer, which is 1 km in the present simulations. Four different tip-speed ratios, i.e., $\lambda = 6.8,\ 7.8,\ 8.8$, and 9.3, are simulated to represent four different operating conditions. The case with $\lambda = 7.8$ represents the condition close to optimal. It is noted that the different tip-speed ratios are realized in the simulations by changing the rotor rotational speed instead of the incoming wind speed. Figure 1 shows the power and thrust coefficients for different tip-speed ratios. It is seen that the C_P increases as the tip-speed ratio increases but starts decreasing from $\lambda = 7.8$. The C_T increases monotonically as the tip-speed ratio increases from 6.8 to 9.3. In the next section, we will examine how these changes in the turbine operating condition affect the turbine wake statistics. Besides the turbine wake simulations, a case without a turbine is also simulated to provide the reference point for analyzing the turbine wake statistics. This no turbine case employs exactly the same grid, time step, and inflow condition as the cases with the turbine. The size of time step is $\Delta t = 0.002D/U_h$ for all the cases. The flowfields are averaged for about 900 rotor revolutions after the flow is fully developed. This averaging time is significantly longer than that in Refs. [21,22,47,48], and is sufficient to obtain converged statistics of the turbine wakes and capture the low-frequency motion of the wake. However, it is still not long enough for the incoming flow statistics to be uniformly distributed in the spanwise direction because of the large temporal scale of the large-scale flow structures captured by the large computational domain employed in the precursory inflow simulation, which will be described in the next paragraph. Further averaging can be performed. However, the disk storage becomes an issue as each case already occupied more than 4.7 TB.

The incoming turbulent flow at the inlet is generated from a precursory simulation with periodic boundary conditions in the horizontal directions. Free slip boundary condition is applied at the top boundary. At the wall, the nonpenetration boundary condition is applied to the wall-normal velocity component; for the wall-tangential velocity component, the shear stress boundary boundary condition is applied with the wall shear stress computed using the logarithmic law for rough walls, i.e., $\frac{\langle u \rangle}{u^*} = \frac{1}{\kappa} \ln\left(\frac{z}{z_0}\right)$, where $\kappa = 0.4$, $u^* = \sqrt{\tau_w/\rho}$ (τ_w is the wall shear stress), the roughness length $z_0 = 0.25$ m for the present cases, and $\langle u \rangle$ is given by the first off-wall grid node. The size of the computational domain for the precursory simulation is 6.2δ, 4.6δ and δ ($\delta = 1$ km is the thickness of the boundary layer) in the downwind (x), spanwise (y), and vertical (z) directions, respectively. The size of the computational domain is chosen to be large enough to capture large coherent structures in the atmospheric boundary layer. The number of grid nodes are $N_x \times N_y \times N_z = 1291 \times 1148 \times 133$. The grid nodes are stretched in the vertical direction with first off-wall grid spacing $\Delta z = 0.0039\delta$. In the horizontal directions, the grid nodes are uniformly distributed. The velocity field on a y-z plane is saved at every time step for the inlet boundary condition in the turbine simulations. The size of the time step employed in the inflow simulation is $0.03D/U_h$. The grid distribution on the y-z plane in the inflow simulation is different from that in the turbine simulations. Linear interpolation

in both time and space is employed to obtain the velocities at the inlet of the turbine simulations. It is also noted that the spanwise dimension of the inflow simulation domain is significantly larger than that of the turbine simulation. Only a portion of the saved y-z plane flowfields from the inflow simulation is used in the turbine simulations.

IV. RESULTS

In this section, we present the computed results from the simulated cases. First we show in Fig. 2 the inflow employed in turbine wake simulations. Figures 2(a) and 2(b) show the time-averaged downwind velocity and TKE fields on the y-z plane in the precursory simulation employed for inflows for the turbine wake simulations. It is seen that mild variations in the spanwise direction exist for both the mean downwind velocity and the TKE fields. For the portion employed for turbine simulations, the incoming wind speed is lower at negative y locations. The TKE levels are similar at different spanwise locations for $z < 3D$, while are higher in the negative y region for $z > 3D$. Figures 2(c)–2(f) show the mean downwind velocity and TKE profiles at the inlet of the turbine simulation domain. In Fig. 2(c), it is seen that the computed vertical profile of the mean downwind velocity agrees well with the logarithmic law. Figure 2(d) shows that the TKE gradually decreases in the vertical direction from the peak at the near wall location. This figure also reveals the magnitude and variation of the TKE across the rotor plane in the vertical direction. Figure 2(e) shows the spanwise variation of the time-averaged downwind velocity at the turbine hub height. It is seen that the time-averaged downwind velocity slightly varies in the spanwise direction. The velocity at $y > 0$ locations is larger than that at $y < 0$ locations with the downwind velocity at $y = 4R$ being about 6% larger than that at $y = -4R$. Figure 2(f) shows the spanwise variation of the TKE at turbine hub height. In the remainder of this section, we will show how such spanwise heterogeneity in the incoming wind and varying turbine operating conditions affect the wake statistics.

Figure 3 depicts the instantaneous downwind velocity fields for cases with different tip-speed ratios. As seen, the cases with higher tip-speed ratios show, as expected, slightly longer wakes because of higher thrust coefficients. Despite of the differences in small-scale structures, similarity in large-scale structures is observed between different cases. We now proceed to examine time and disk-averaged quantities to to investigate how wake recovers and how TKE varies in the downwind direction as a function of tip-speed ratios. The disk used for averaging is of the same radius as the rotor and is located on the y-z plane at different downwind locations. Figure 4 shows the variation of time and disk-averaged downwind velocity at different downwind locations. As seen, increasing the tip-speed ratio from 7.8 decreases the downwind velocity until about $5D$ downwind of the turbine. Decreasing the tip-speed ratio from 7.8 to 6.8, however, increases the downwind velocity at almost all considered downwind locations. Therefore, it is reasonable to speculate that lowering the tip-speed ratio of the upwind turbine may increase the power of two turbines compared to the situation when the upwind turbine is operating optimally. Figure 5 shows the downwind variation of (a) the disk-averaged turbulence intensity and (b) the maximum turbulence intensity within the disk for the three components of velocity fluctuations. As seen, increasing the tip-speed ratio from 7.8 increases the turbulence intensity at different downwind locations. Decreasing tip-speed ratio from 7.8 to 6.8 decreases the turbulence intensity except for the disk-averaged downwind component of the turbulence intensity, which increases in the near wake ($x < 2D$). It is seen that the maximum turbulence intensity in the disk is significantly higher than the disk-averaged value especially for the downwind component of the turbulence intensity, which is more than 35% higher.

We now examine the velocity deficit and turbine-added TKE profiles computed based on wake center locations. The velocity deficit and TKE profiles are computed from the time series of spanwise and vertical profiles passing through $z = z_h$ and $y = 0$, respectively, at different turbine downwind locations, which are extracted from the flowfields saved for every 20 time steps (which means that the time increment is $0.04D/U_h$ between two successively saved flowfields). The velocity deficit Δu and turbine-added TKE Δk are computed by subtracting those from the simulation

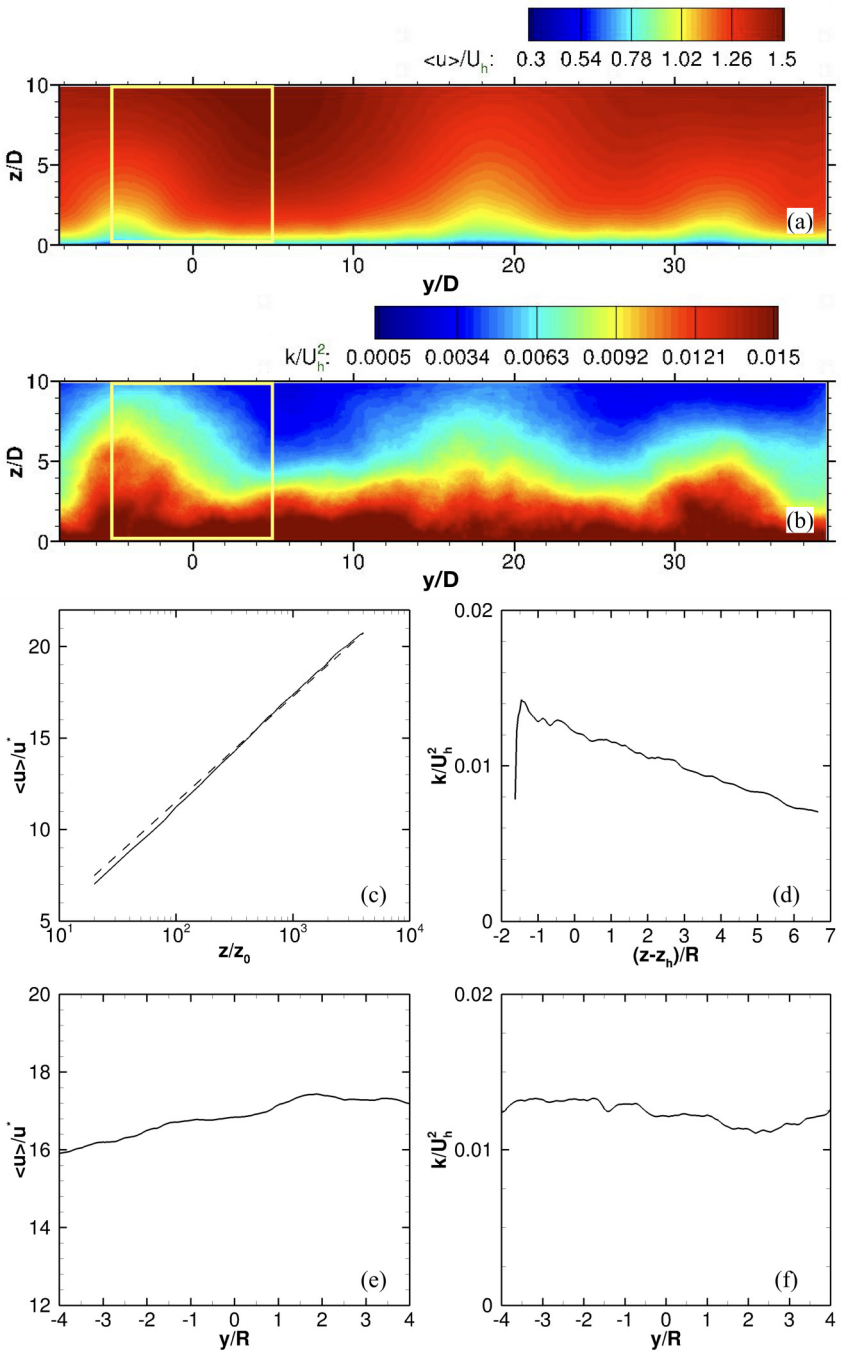

FIG. 2. Statistics of the inflow. (a) and (b) contours of the time-averaged downwind velocity and TKE, respectively, on the y-z plane from the inflow simulation, where the instantaneous flowfields are saved for the wind turbine simulation; (c) vertical profiles of the downwind velocity $\langle u \rangle$ (solid line) averaged in time and the spanwise direction and the logarithmic law $\frac{\langle u \rangle}{u^*} = \frac{1}{\kappa} \ln\left(\frac{z}{z_0}\right)$ (dashed line), (d) the vertical profile of the TKE k averaged in time and the spanwise direction, (e) the spanwise profile of the time-averaged downwind velocity at turbine hub hight ($z = z_h$), and (f) the spanwise profile of the TKE k at turbine hub hight ($z = z_h$). The yellow boxes in (a) and (b) show the part employed in turbine simulations.

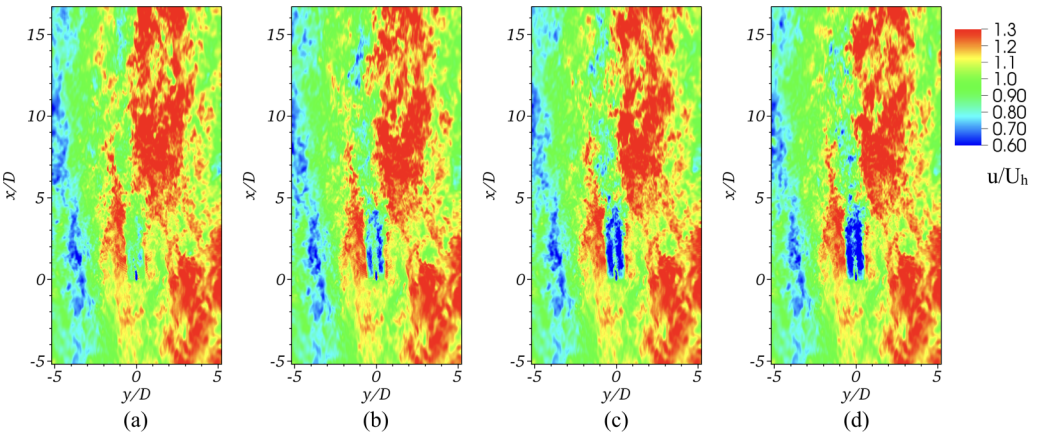

FIG. 3. Contours of the instantaneous downwind velocity on the horizontal plane located at turbine hub height for (a) $\lambda = 6.8$, (b) $\lambda = 7.8$, (c) $\lambda = 8.8$, and (d) $\lambda = 9.3$, respectively.

without a turbine as follows:

$$\Delta u = u_{\mathrm{NT}} - u \tag{9}$$

for velocity deficits, and

$$\Delta k = k - k_{\mathrm{NT}} \tag{10}$$

for TKE, respectively, where the downwind velocity and TKE with a subscript NT and without a subscript are from the simulations without a turbine and with a turbine, respectively. To compute the quantities based on wake center positions, three regions are identified, i.e., $y_c < -R$, $-R \leqslant y_c \leqslant R$, and $y_c > R$ in the spanwise direction, and $z_c - z_h < -R$, $-R \leqslant z_c - z_h \leqslant R$, and $z_c - z_h > R$ in the vertical direction, respectively, where y_c and z_c are the coordinates of the wake center position in the spanwise and vertical directions, respectively. The wake center is identified as the location where the maximum Δu occurs using the instantaneous velocity deficit profiles passing through the rotor centerline. To reduce the effects of the small-scale flow structures on identifying wake centers, the Δu profiles are filtered using a top-hat filter. Three different filter widths of $0.25D$, $0.5D$, and D are tested to examine the effects of filter width on identifying wake centers. The identified wake center

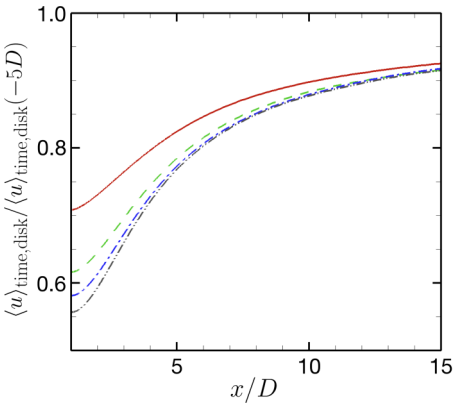

FIG. 4. Variation of time and disk-averaged downwind velocity at different downwind locations. Red solid line, $\lambda = 6.8$; green dashed line, $\lambda = 7.8$; blue dash-dot line, $\lambda = 8.8$; gray dash-dot-dot line, $\lambda = 9.3$.

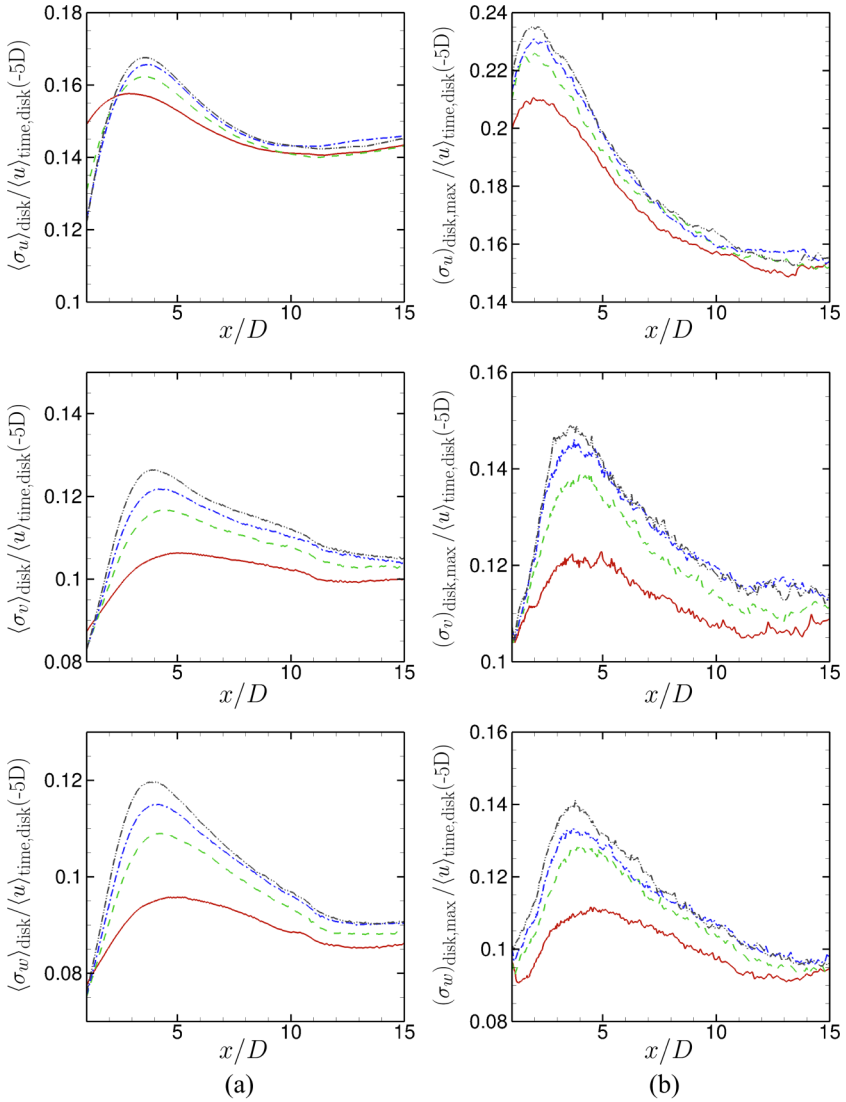

FIG. 5. Downwind variation of (a) the disk-averaged turbulence intensity and (b) the maximum turbulence intensity within the disk for the three components of turbulence intensity, i.e., σ_u, σ_v, and σ_w for the downwind, spanwise, and vertical components, respectively. Red solid line, $\lambda = 6.8$; green dashed line, $\lambda = 7.8$; blue dash-dot line, $\lambda = 8.8$; gray dash-dot-dot line, $\lambda = 9.3$. (a) $\langle\sigma_{u,v,w}\rangle_{\rm disk}$ and (b) $(\sigma_{u,v,w})_{\rm disk,max}$.

locations are observed to be similar for the three filter widths except at the near wake location, i.e., $x = 2D$. In the following results, the filter width $0.5D$ is adopted as in our previous work [21,27,32].

We show the spanwise and vertical velocity deficit profiles in Figs. 6 and 7, respectively. It is seen that the velocity deficit profiles averaged when $-R < y_c < R$ [Fig. 6(b)] are very similar to those averaged for all wake center locations [Fig. 6(a)] and of Gaussian shape at far wake locations. The velocity deficit profiles averaged for wakes centers in the other two regions [Figs. 6(c) and 6(d)], however, are very different and no longer of Gaussian shape. It is also observed that the velocity deficits averaged when $y_c < -R$ are larger, which is because of the lower incoming wind speed in the $y < -R$ region. Although the differences between cases of different tip-speed ratios are significant at near wake locations, it is noticed that such differences become negligible at far wake locations.

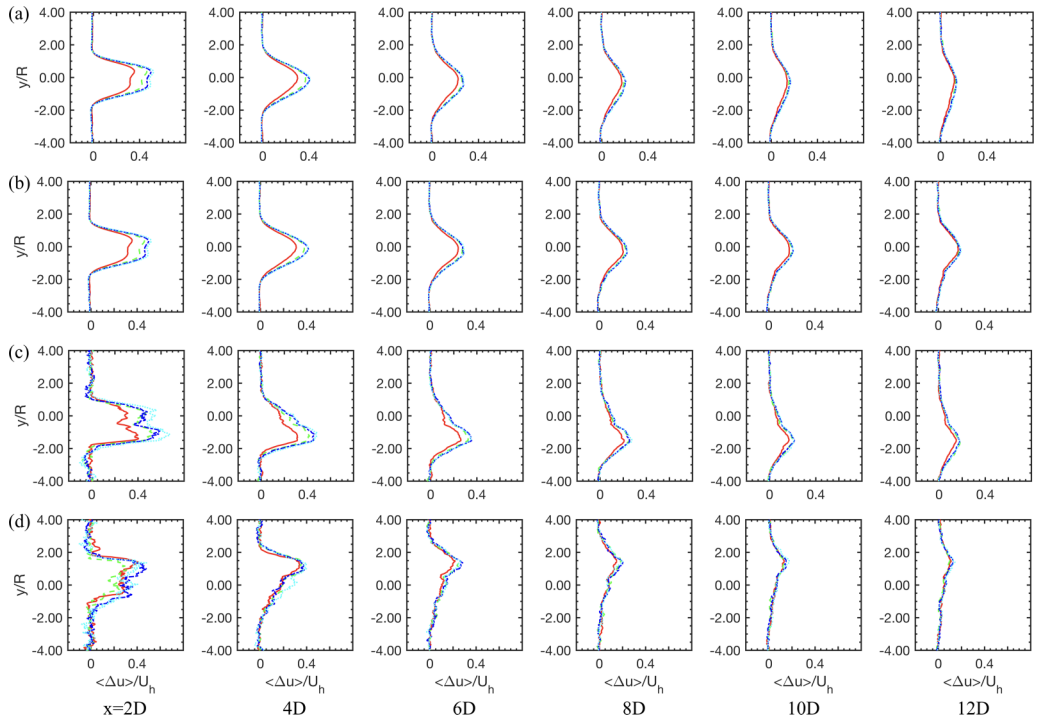

FIG. 6. Spanwise profiles of velocity deficits $\langle \Delta u \rangle$ for (a) averaged for all wake center locations, and (b)–(d) averaged when $-R \leqslant y_c \leqslant R$, $y_c < -R$, and $y_c > R$, respectively, at different downwind locations. Red solid line, $\lambda = 6.8$; green dashed line, $\lambda = 7.8$; blue dash-dot line, $\lambda = 8.8$; cyan dotted line, $\lambda = 9.3$.

The vertical velocity deficit profiles averaged when $-R < z_c - z_h < R$ [Fig. 7(b)] are also observed to be very similar with that averaged for all wake center locations [Fig. 7(a)]. It is also observed that the vertical velocity deficit profiles for different tip speed ratios are very similar with each other at far wake locations. Because of the wall blocking effect, the velocity deficit profiles averaged when $z_c - z_h < -R$ [Fig. 7(c)] are observed to be different from those averaged for wake centers in the other regions. At $x = 6D$, $8D$, $10D$, and $12D$ turbine downwind locations, it is seen that the vertical velocity deficit profiles averaged when $z_c - z_h < -R$ are composed of two parts, i.e., the nearly linear part in the $-0.5R < z - z_h < R$ region and the part in the $-1.5R < z - z_h < -0.5R$ region, which is a result of the interaction of the wake with the wall.

We now examine the spanwise and vertical turbine-added TKE profiles in Figs. 8 and 9, respectively. In our previous studies, we have shown that normalizing the turbine-added TKE using a velocity scale U_T is able to collapse the turbine-added TKE profiles for different inflows (caused by different hill-turbine distances) [26] and different turbine designs [27]. In this work, we examine if such scaling law still works for the turbine-added TKE computed based on wake center locations and from cases with different tip-speed ratios. Figure 8 shows the spanwise profiles of turbine-added TKE. As seen in Fig. 8(a) for the turbine-added TKE profiles computed for all wake center locations, two peaks around $y = \pm R$ are observed. It is seen that the peak around $y = R$ is significantly higher than that around $y = -R$ at $x = 2D$, $4D$, and $6D$ downwind locations. This is because of the higher incoming wind when $y > R$, which enables faster wake recovery as well as higher TKE. It is also seen that the peak at around $y = -R$ becomes less significant at $x = 8D$ and negligible at further downwind locations. Figure 8(b) shows the turbine-added TKE profiles computed when $-R < y_c < R$. As seen, these profiles are very similar to those computed for all wake center locations as shown in Fig. 8(a). Figure 8(c) shows the turbine-added TKE profiles computed when $y_c < -R$. As those profiles in Figs. 8(a) and 8(b), two peaks are observed at near

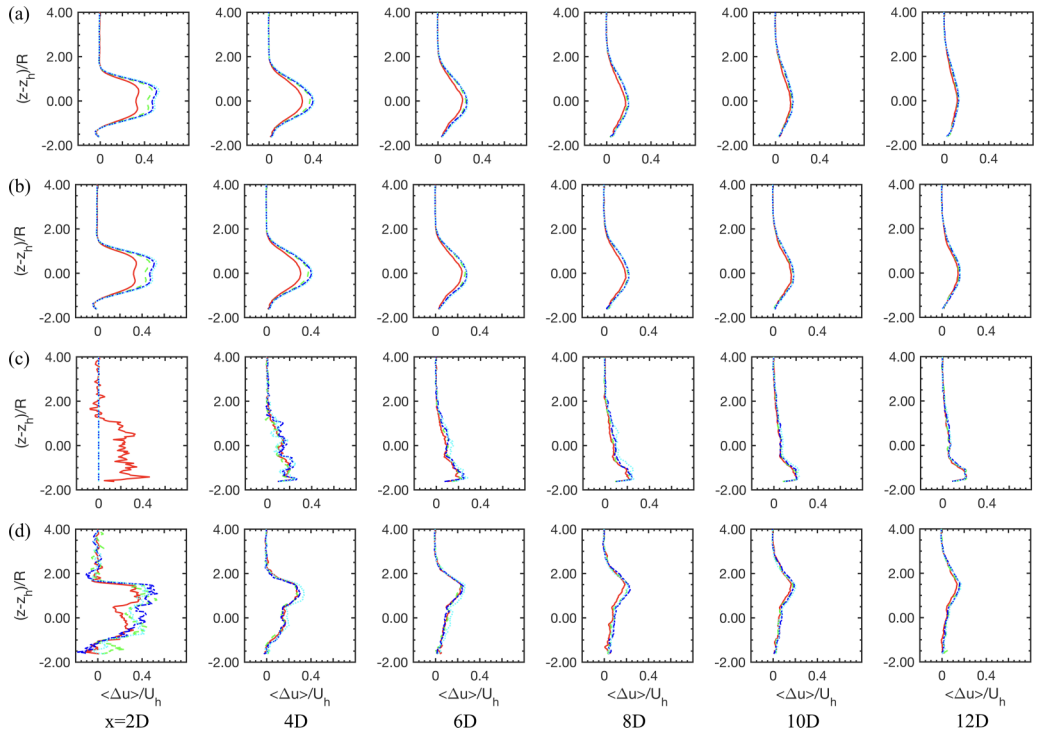

FIG. 7. Vertical profiles of velocity deficits $\langle \Delta u \rangle$ for (a) averaged for all wake center locations, and (b)–(d) averaged when $-R \leqslant (z_c - z_h) \leqslant R$, $z_c - z_h < -R$, $z_c - z_h > R$, respectively, at different downwind locations. Red solid line, $\lambda = 6.8$; green dashed line, $\lambda = 7.8$; blue dash-dot line, $\lambda = 8.8$; cyan dotted line, $\lambda = 9.3$.

wake locations. However, their locations are shifted in the negative y direction to around $y = 0.5R$ and $y = -2R$ locations, respectively. Figure 8(d) shows the turbine-added TKE profiles computed when $y_c > R$, where the incoming wind is higher as shown in Fig. 2. At $x = 4D$ three peaks at approximately $y = -R$, R, $2R$ are observed for the three higher tip-speed ratio cases with the one located around $y = R$ disappearing at $x = 6D$. One interesting observation from this figure is that the peaks of the turbine-added TKE persist at much further downwind locations compared with Figs. 8(a)–8(c), which indicates that the entrainment of high speed wind into the wake is still active at these far wake locations when $y_c > R$. Figure 9 shows the vertical profiles of the turbine-added TKE. Different from Fig. 8, only one peak around $z = z_h + R$ exists in the vertical direction at the considered downwind locations. As moving in the downwind direction, the profiles are very similar to each other although the magnitude of TKE decreases. The turbine-added TKE profiles computed when $-R < z_c - z_h < R$ are shown in Fig. 9(b). It is seen that the turbine-added TKE profiles in Fig. 9(b) are very similar to that in Fig. 9(a), although the magnitudes of TKE are somewhat lower in Fig. 9(b) at far wake locations. The turbine-added TKE profiles computed when $z_c - z_h < -R$ are shown in Fig. 9(c). One interesting observation [which is also observed in Figs. 8 and Figs. 9(a), 9(b), and 9(d) but not as clearly as in Fig. 9(c)] is that the Δk values are negative in the $z - z_h < -R$ region, which indicates that the turbine wake suppresses the turbulent fluctuations near the wall. The turbine-added TKE profiles computed when $z_c - z_h > R$ are shown in Fig. 9(d). One major difference compared with Figs. 9(a)–9(c) is that there are two peaks located around $z - z_h = 0$ and $z - z_h = 2R$ locations, respectively, which indicates that significant amount of momentum is entrained into the wake from both the upper and lower boundaries of the wake when $z_c - z_h > R$.Finally, we want to emphasize the most important observation from Figs. 8 and 9

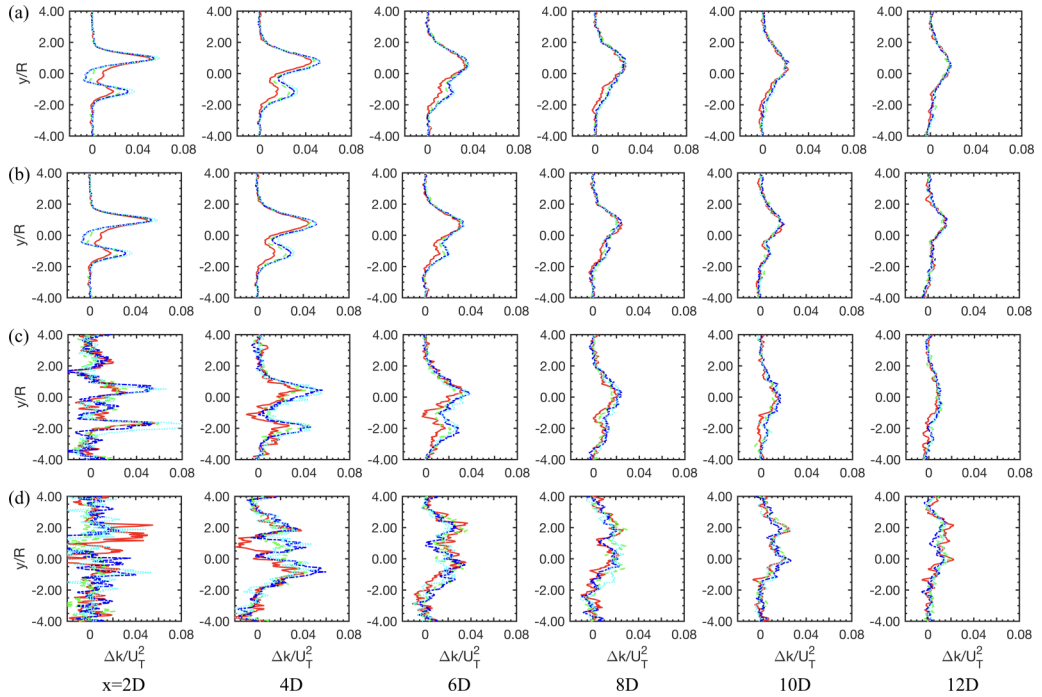

FIG. 8. Spanwise profiles of turbine-added TKE Δk for (a) computed for all wake center locations, and (b)–(d) computed when $-R \leqslant y_c \leqslant R$, $y_c < -R$, and $y_c > R$, respectively, at different downwind locations. Red solid line, $\lambda = 6.8$; green dashed line, $\lambda = 7.8$; blue dash-dot line, $\lambda = 8.8$; cyan dotted line, $\lambda = 9.3$.

is that the turbine-added TKE profiles computed based on wake center locations collapse well with each other at $x = 6D$ and further downwind locations when normalized by U_T.

We have seen the similarity of large-scale flow structures from the instantaneous flowfields as shown in Fig. 3. To further examine such similarity in turbine wakes, we show the power spectral density (PSD) of the spanwise velocity fluctuations along the rotor centerline at different downwind locations in Fig. 10. The PSD is computed using Welch's method [49]. The velocity at every time step (the size of time step is $\Delta t = 0.002D/U_h$) is recorded for computing the PSD. The total number of time steps is 200 000. For the PSD profiles presented in this section, we employ $L = 100\,000$ (the length of each segment), $S = 20\,000$ (the separation between two adjacent segments) and the W_2 window function, which will be defined in the appendix, for computing the PSD using Welch's method. Figure 10 shows the PSD at $2D$ turbine upwind. As seen, a significant amount of energy exists at a very low frequency of $fD/U_h \approx 0.01$ in the inflow. It is interesting to see that this low-frequency motion from the inflow persists at $5D$, $10D$, and $15D$ turbine downwind locations as shown in Figs. 10(b)–10(d), respectively. The PSD levels of the low-frequency motion with $fD/U_h \approx 0.01$ are either increased or decreased at these turbine downwind locations in comparison with that at $x = -2D$. The downwind variations of the PSD levels for different frequencies will be examined in Fig. 11. It should be noticed that the blade passing frequency (which is $fD/U_h \approx 6.3 \sim 8.6$ for the present cases) is not discernible in Figs. 10(b)–10(d) for two reasons: (1) the spanwise velocity fluctuations are recorded at turbine hub height where the wake is dominated by the nacelle wake; and (2) the signature from the rotor's rotational motion is significantly attenuated at $5D$, $10D$, and $15D$ turbine downwind locations. Besides the low-frequency motion from the incoming flow, the wake is also dominated by another relatively higher frequency of $fD/U_h \approx 0.15$ as shown in Figs. 10(b)–10(d), which is the frequency of the large-scale motion of the wake caused by the wake shear layer instability similar to that of the vortex shedding behind bluff

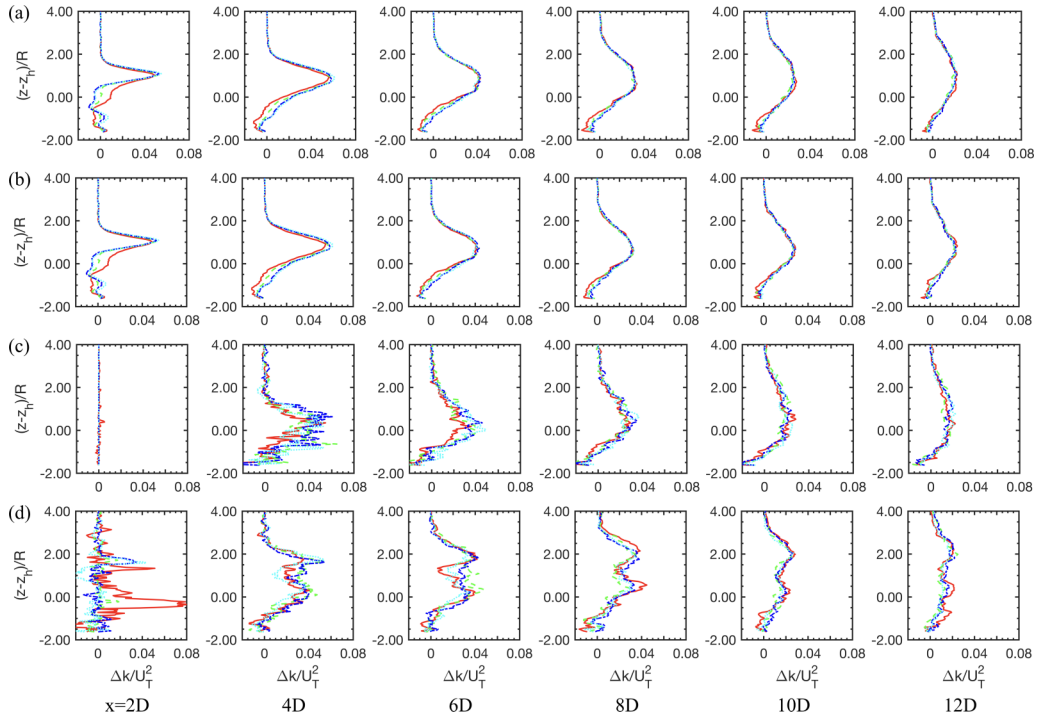

FIG. 9. Vertical profiles of turbine-added TKE Δk for (a) computed for all wake center locations, and (b)–(d) computed when $-R \leqslant (z_c - z_h) \leqslant R$, $z_c - z_h < -R$, $z_c - z_h > R$, respectively, at different downwind locations. Red solid line, $\lambda = 6.8$; green dashed line, $\lambda = 7.8$; blue dash-dot line, $\lambda = 8.8$; cyan dotted line, $\lambda = 9.3$.

bodies. Both frequencies describe the large-scale motion of the turbine wake. In this paper, we refer the wake motion of frequency $fD/U_h \approx 0.15$ as the shear-induced meandering motion, and the wake motion of frequency $fD/U_h \approx 0.01$ as the inflow-driven meandering motion, respectively, for differentiating the large-scale motion of the wake at two different frequencies. Now we examine how the turbine and the wake interact with the incoming turbulence at different scales, i.e., from the large-scale motion at frequency of $fD/U_h \approx 0.01$ to the shear-induced wake meandering motion at frequency of $fD/U_h \approx 0.1 \sim 0.2$ and wake motion at frequencies higher than the frequency of the shear-induced wake meandering motion. To do this, we divide the frequencies into four regions, i.e., $fD/U_h \leqslant 0.02, 0.02 < fD/U_h \leqslant 0.14, 0.14 < fD/U_h \leqslant 0.2$, and $0.2 < fD/U_h \leqslant 0.32$, which we denote as low, intermediate, shear-induced meandering, and high frequencies, respectively. In each region, the maximum PSD at each downwind location is found and plotted in the right column of Fig. 11 with the corresponding frequency plotted in the left column of Fig. 11, respectively. First we examine the downwind variation of the frequencies with the maximum PSD level in the left column of Fig. 11. We can see on the left of Fig. 11(a) that the dominant frequency in the low-frequency region (frequency of the inflow-driven meandering at far wake locations) persists at $fD/U_h \approx 0.01$ for most downwind locations until $x = 10D$, and shifts to a higher value at further downwind locations for some cases. The shear-induced meandering frequency as shown on the left of Fig. 11(c) stays at around $fD/U_h \approx 0.15$ starting from $x = 3D \sim 4D$ for all the cases. The dominant frequencies in the other two regions, however, fluctuate vibrantly for all the cases as shown on the left in Figs. 11(b) and 11(d). Now we examine the downwind variation of the maximum PSD level in the right column of Fig. 11. The PSD level of the low-frequency motion (inflow-driven meandering at far wake locations) at $fD/U_h \approx 0.01$ decreases until $x \approx 2D$ to about 50% of that at $x = -2D$. The PSD levels in the regions of intermediate frequency, shear-induced meandering

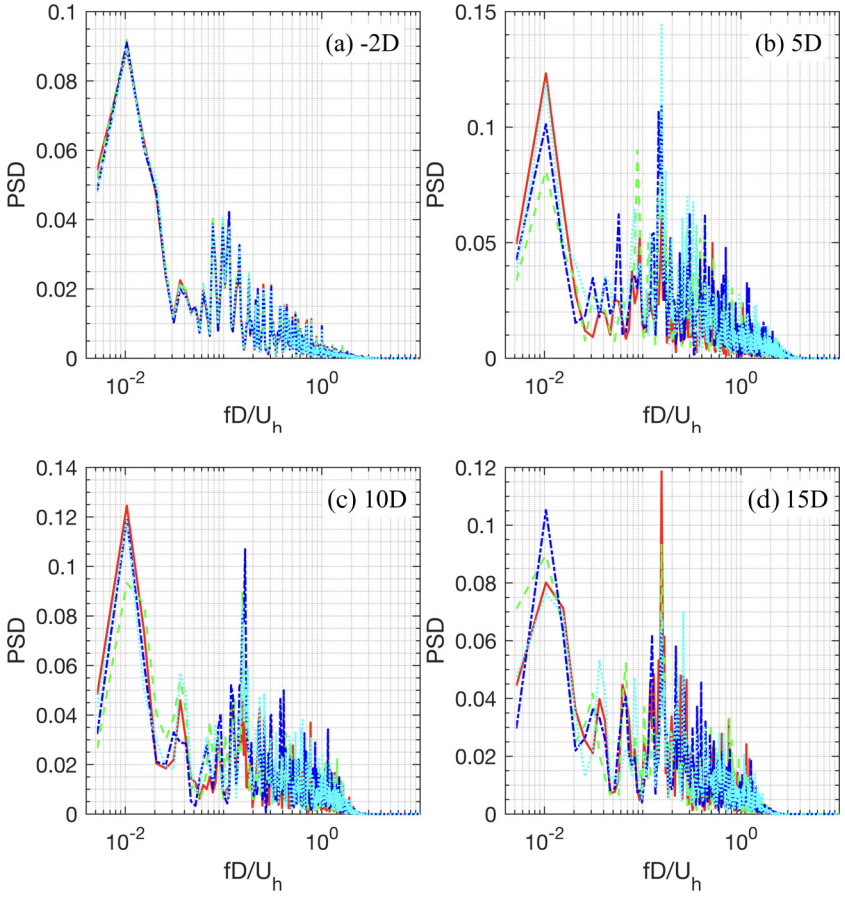

FIG. 10. PSD profiles from cases of different tip-speed ratios at different downwind locations. The PSD is computed using the spanwise velocity fluctuations at different turbine downwind locations along the rotor centerline and normalized by the variance at $x = -2D$. Red solid line, $\lambda = 6.8$; Green dashed line, $\lambda = 7.8$; Blue dash-dot line, $\lambda = 8.8$; Cyan dotted line, $\lambda = 9.3$.

frequency and high frequency, however, increase as approaching the turbine and decrease to the minimum at $x \approx 2D$. From $x \approx 2D$ the maximum PSD levels in the four frequency regions start increasing to a plateau at around $x \approx 4D \sim 5D$. The PSD levels at $x > 4D$ locations are similar for different cases, except that the PSD levels of the $\lambda = 6.8$ case are smaller than the other cases in the intermediate and shear-induced meandering frequency regions for $5D < x < 12D$.

So far we have examined the disk-averaged statistics, statistics based on wake center locations, and the PSD of velocity fluctuations for different operating conditions. Now we investigate the statistics of wake center locations, which are useful for developing the wake steering technique to alleviate the negative impacts of wakes on downwind turbines. As mentioned, the velocity deficits defined as $\Delta u = u_{\mathrm{NT}} - u$ [with the mean plotted in Figs. 6(a) and 7(a)] are used to detect wake center locations. Figure 12 shows the wake center locations at different downwind locations for the entire simulation time for tip speed ratio $\lambda = 7.8$. In this figure, the wake center is identified as the location of the maximum of the instantaneous velocity deficits Δu on y-z planes at different downwind locations. To reduce the uncertainties, a spatial filtering on the y-z plane with the filter width of $0.5D$ is performed on the instantaneous velocity deficit field similar to the work in Refs. [19,21]. As seen at the near wake locations ($x < 3D$), the wake center positions are confined within a small circle of radius less than the rotor radius. The region having wake centers gradually

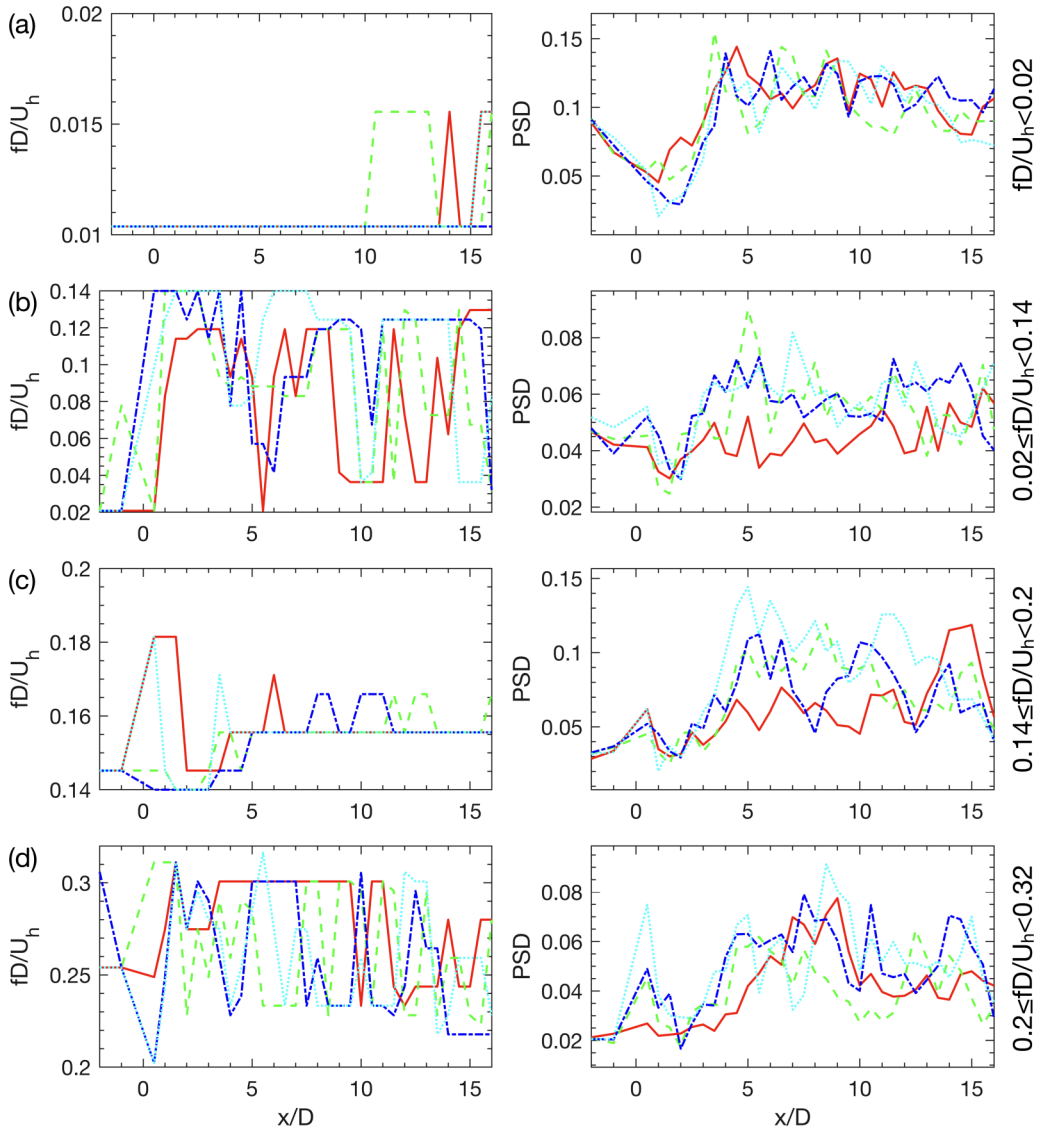

FIG. 11. Downwind variations of the maximum PSD and the corresponding frequency in the four regions of different ranges of frequency for (a) $0.01 \leqslant fD/U_h < 0.02$, (b) $0.02 \leqslant fD/U_h < 0.14$, (c) $0.14 \leqslant fD/U_h < 0.2$, and (d) $0.2 \leqslant fD/U_h < 0.32$, respectively. The PSD is computed using the spanwise velocity fluctuations at different downwind locations along the rotor centerline and normalized by the variance at $x = -2D$. Red solid line, $\lambda = 6.8$; Green dashed line, $\lambda = 7.8$; Blue dash-dot line, $\lambda = 8.8$; Cyan dotted line, $\lambda = 9.3$. It is noticed that the data are sampled every $0.5D$ and $1D$ in the turbine downwind and turbine upwind direction, respectively.

increases in both spanwise and vertical directions in the downwind direction. Starting from $x \approx 4D$, the radius of the wake center region is larger than the rotor radius while from around $x = 6D \sim 7D$ wake centers are detected in the near wall region as a result of wake expansion and its interaction with the wall. Starting from around $x = 6D \sim 7D$, the radius of the wake center area in the spanwise direction is observed to be larger than the rotor diameter. At very far downwind locations (e.g., $x > 13D$), the wake center area ranges approximately $-2D < y < 2D$ and $0 < z < 1.5D$ in the

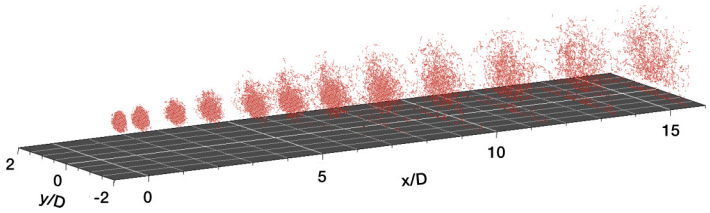

FIG. 12. Scattered points showing instantaneous wake center locations at different downwind locations for the entire simulation time. Tip-speed ratio $\lambda = 7.8$.

spanwise and vertical directions, respectively. Our simulations reveal similar wake center scattering as in Fig. 12 for the other different tip-speed ratios.

Subsequently, we compare the PDF profiles of wake center locations in the spanwise and vertical directions. Figure 13 shows the PDF of wake center locations in the spanwise direction at different downwind locations. The thick black line in each subplot shows the fitted Gaussian distribution. At $2D$ turbine downwind, some deviations from the Gaussian distribution are observed near the peak of the PDF. At $4D$ and $6D$ downwind locations, an overall good agreement of the computed PDF with the Gaussian distribution is observed although some minor differences are still observed. At $x = 8D$ and further downwind locations, the differences between the computed PDF and the fitted Gaussian distribution are significant. As seen, the computed PDF indicates a higher probability for the wake centers in the region around the mean wake center while a lower probability in the region away from the mean wake center compared with the fitted Gaussian distribution. Similar field observation but at 4D turbine downwind was reported in Ref. [50]. At $x = 12D$, the computed PDF is also significantly skewed that the wake centers have a lower probability in the positive y side than in the negative y side. Figure 14 shows the PDF of wake center locations in the vertical direction at different downwind locations. The same as in Fig. 13, the computed PDF slightly deviates from

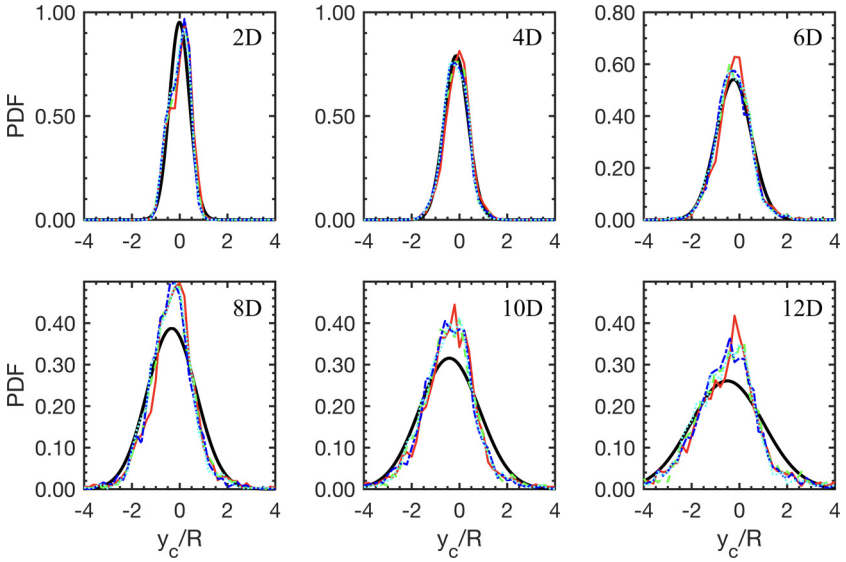

FIG. 13. PDF of wake center locations in the spanwise direction at turbine hub height and different turbine downwind locations. Red solid lines, $\lambda = 6.8$; green dashed lines, $\lambda = 7.8$; blue dash-dot lines, $\lambda = 8.8$; cyan dotted lines, $\lambda = 9.3$. The thick black lines represent the fitted Gaussian distribution with the mean and standard deviation averaged from four cases.

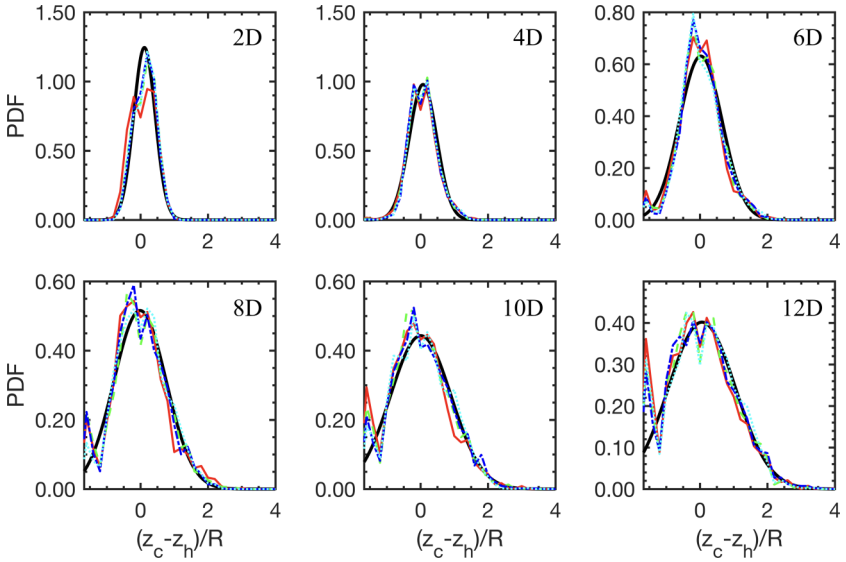

FIG. 14. PDF of wake center locations in the vertical direction along the rotor centerline at different turbine downwind locations. Red solid lines, $\lambda = 6.8$; green dashed lines, $\lambda = 7.8$; blue dash-dot lines, $\lambda = 8.8$; cyan dotted lines, $\lambda = 9.3$. The thick black lines represent the fitted Gaussian distribution with the mean and standard deviation averaged from four cases.

the Gaussian distribution around the peak of the PDF at $2D$ turbine downwind location especially for the $\lambda = 6.8$ case. At $x = 4D$ turbine downwind location the Gaussian distribution reasonably approximates the computed PDF although some minor differences are still observed. The probability for wake centers in the region close to ground is observed to be high at $x = 6D$ turbine downwind location and gradually increases at further turbine downwind locations. The PDF in the near ground region cannot be modeled by the Gaussian distribution, though the Gaussian distribution seems to be an acceptable approximation in the region away from the ground. From Figs. 13 and 14, we can see that the Gaussian distribution is an acceptable approximation to the computed PDF distributions at $x = 2D$, $4D$, and $6D$. At $x = 8D$ and further downwind locations, significant differences between the Gaussian distribution and computed PDF distributions are observed. In spite of the different fitness of the computed PDF to the Gaussian distribution at different downwind locations, the computed PDF from different cases collapse well with each other at almost all considered downwind locations.

To further quantify how well the PDF of wake center locations can be represented by the Gaussian distribution, we plot in Fig. 15 the skewness and kurtosis of wake center locations. First we examine the skewness and kurtosis of wake center fluctuations in the spanwise direction as shown in Figs. 15(a) and 15(c), respectively. As seen the values of skewness and kurtosis from different cases are similar to each other and close to 0 and 3, respectively, for $x < 5D$, indicating that in this region the PDF of wake center locations can be reasonably represented by the Gaussian distribution. For $x > 5D$, however, the skewness and kurtosis from different cases are much scattered and significantly deviate from 0 and 3, respectively, which means that the Gaussian distribution is not a proper choice in this region. In Figs. 15(b) and 15(d) we examine the skewness and kurtosis of wake center fluctuations in the vertical direction. Similar trends with that in the spanwise direction are observed. However, the skewness and kurtosis become scattered at about $x = 9D$ much later than the spanwise direction.

After examining the PDF of the wake center locations, we show the downwind variations of the mean wake center locations and the standard deviation of wake center fluctuations in Fig. 16. First we examine the mean of wake center locations in Figs. 16(a) and 16(b). As seen the mean

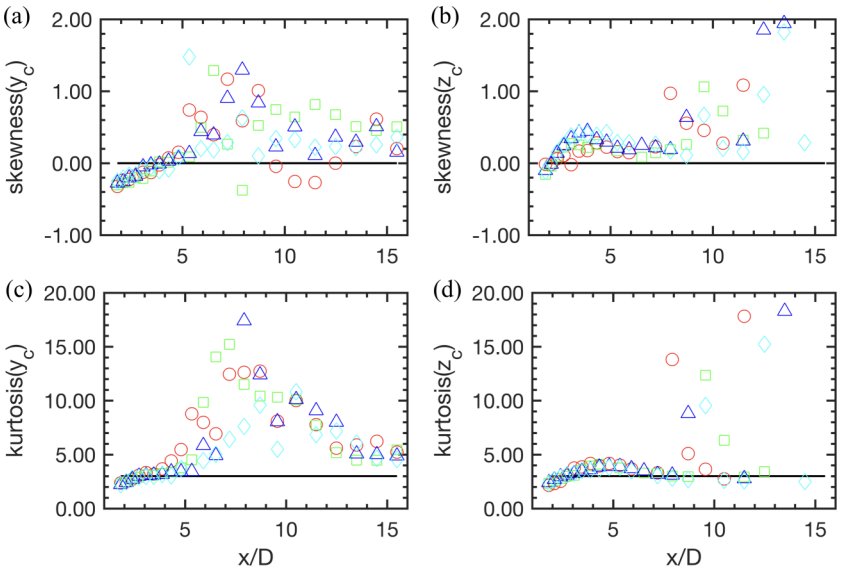

FIG. 15. Skewness and kurtosis of wake center locations for (a) and (c) in the spanwise direction and (b) and (d) in the vertical direction, respectively, at different downwind locations. Red circles, $\lambda = 6.8$; green squares, $\lambda = 7.8$; blue triangles, $\lambda = 8.8$; cyan diamonds, $\lambda = 9.3$.

wake center moves to the negative y direction as the wake travels in the downwind direction. This is because of the spanwise heterogeneous distribution of the incoming wind which is higher at the positive y side compared with that at the negative y side. It is interesting to see that the slope is

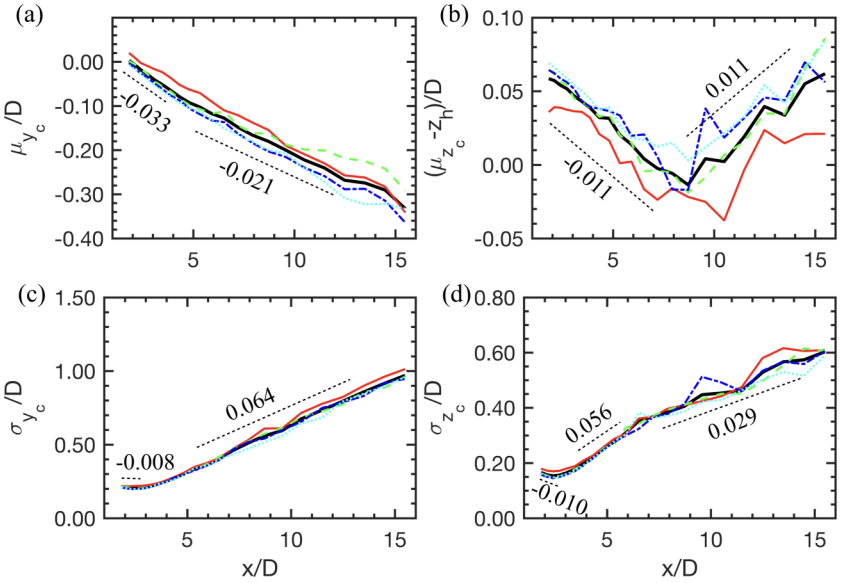

FIG. 16. Mean and standard deviation of wake center locations for (a) and (c) in the spanwise direction and (b) and (d) in the vertical direction, respectively, at different downwind locations. Red solid lines, $\lambda = 6.8$; green dashed lines, $\lambda = 7.8$; blue dash-dot lines, $\lambda = 8.8$; cyan dotted lines, $\lambda = 9.3$. The thick black lines represent the Gaussian fitted mean and standard deviation averaged over the four cases. The black dashed lines show the best-fitted slopes of the thick black lines.

nearly constant, although it is somewhat higher from $2D$ to $4D$ turbine downwind. Figure 16(b) shows the downwind variation of the wake centers in the vertical direction. As seen two stages exist for the downwind variations of wake centers z_c. From $1D$ turbine downwind to $9D$ turbine downwind the wake centers move toward the wall, while from $9D$ to $16D$, the wake centers move away from the wall. It is noticed that at $x = 9D$, where the wakes bounce away from the ground, is exactly the same location where the skewness and kurtosis of the vertical wake center locations become scattered as shown in Figs. 15(b) and 15(d). This observation is similar for cases of different tip-speed ratios except for the case of tip-speed ratio $\lambda = 6.8$, for which the minimum wake center in the vertical direction is much lower than the other cases and happens at much further turbine downwind location (about $10D$ to $11D$). It is also noticed that the magnitudes of the slopes are nearly the same for the two stages. In Fig. 16(c), we show the downwind variations of the standard deviations of the wake center fluctuations in the spanwise direction. Two stages similar with that in Fig. 16(a) are observed. In the first stage σ_{y_c} remains nearly the same from $2D$ to about $4D$ turbine downwind, where the wake meandering has not yet started and wake centers fluctuate in a very confined region. In the second stage from $x = 4D$, a linear increase is observed. Figure 16(d) shows the downwind variations of the standard deviations of wake center fluctuations in the vertical direction. Different from Figs. 16(a) and 16(c), three stages are observed. The first stage is very similar to that in Fig. 16(a), where σ_{z_c} remains nearly constant from $2D$ to $4D$ turbine downwind. In the second stage from $4D$ to about $7D$ turbine downwind, σ_{z_c} grows linearly at a rate similar to that in the second stage of Fig. 16(c). In the third stage, however, σ_{z_c} grows linearly at a rate about half of the rate of the second stage from $7D$ until $16D$ turbine downwind. For the downwind variations of both the mean center locations and the standard deviations of the wake center fluctuations, one important observation is that the profiles collapse well with each other for the four different cases with different operating conditions. Such similarity implies scaling laws for describing the downwind variations of the mean wake center locations and the standard deviation of the wake center fluctuations. Development of such scaling laws will be carried out based on wake data from different turbines, operating conditions and inflow conditions in our future work.

V. CONCLUSIONS

We investigated the wake of the EOLOS 2.5 MW Clipper turbine under different operating conditions using LES with the actuator surface models for turbine blades and the nacelle. Four cases with different tip-speed ratios and one case without a turbine under exactly the same inflow were carried out. The inflow was generated from a precursory simulation using a very large computational domain to include the large-scale flow structures existing in the atmospheric turbulence. The velocity deficits and the turbine-added TKE computed based on different wake center locations were analyzed. We found that the velocity deficit profiles and the turbine-added TKE profiles computed for wake centers directly in the downwind of the turbine are nearly the same as those computed for all wake center locations, while those computed when wake centers are above the top tip, below the bottom tip, or off the tips in the spanwise direction are significantly different. At far wake locations (starting from about $6D$ turbine downwind) we found that the incoming wind speed at the turbine hub height and the velocity defined by the thrust on the rotor are the proper velocity scales for the velocity deficits and turbine-added TKE computed based on different wake center locations for all tip-speed ratio cases. We investigated the power spectral density (PSD) from different cases and found that the frequency of the large-scale flow structures from the inflow persists in the turbine wake at different turbine wake locations for all cases, which indicates the large-scale motion of turbine wakes caused by the inflow large-scale eddies, the so-called inflow-driven wake meandering in the present paper. The other dominant frequency of the large-scale motion of turbine wakes is also observed at turbine far wake locations starting at about $3D \sim 4D$ turbine downwind for all the cases. The second dominant frequency is of Strouhal number 0.15 typical for the frequency of vortex shedding behind bluff bodies, which indicates the wake shear layer instability also causes the large-scale motion of turbine wakes, the so-called shear-induced wake meandering in the present

paper. We further divide a range of frequency into four regions, i.e., the low-frequency region where the frequency of the inflow large-scale flow structures is located, the intermediate frequency region of frequencies higher than the incoming low frequency but lower than the frequency of the shear-induced wake meandering, the frequency region of the shear-induced wake meandering, and the high frequency region with frequencies higher than the frequency of shear-induced meandering. It is observed that the PSD level of the inflow low-frequency motion decreases as approaching the turbine and in the turbine's near wake, which was recently observed in the measurements and termed the sheltering effect of the turbine [51]. At far wake locations ($x > 4D \sim 5D$) the maximum PSD levels in the four regions are increased for all the cases except for the $\lambda = 6.8$ case, in which the increases are not significant in the intermediate and the shear-induced meandering frequency regions. We also investigated the profiles of probability density function (PDF) of the wake center locations at different downwind locations. We found that the PDF profiles from all the cases of different tip-speed ratios collapse with each other for almost all the downwind locations. At $2D$, $4D$, and $6D$ turbine downwind locations, the PDF profiles can be reasonably approximated by the Gaussian distribution. At further turbine downwind locations, however, the PDF profiles deviate from the Gaussian distribution. To further test the validity of the Gaussian distribution for the PDF of wake center locations, the skewness and kurtosis of the wake center fluctuations were examined. Finally, we examined the downwind variations of the mean values and the standard deviations of wake center fluctuations and found that they collapse with each other for all the considered tip-speed ratios.

In this study, the employed incoming wind is somewhat lower in the $y/R < 0$ region (the turbine is located at $y/R = 0$). This causes a higher probability for wake centers in the $y/R < 0$ region, which then affects the wake statistics that depend on the spanwise locations (Figs. 6, 8, and 13). However, this does not affect the similarity we observed from different tip-speed ratio cases as the inflow applied is exactly the same. The computed results also indicate the possibility to model the inflow effect on the spanwise wake center displacement as shown in Fig. 16, which is useful for computing wake statistics for a period of time not long enough, or turbines in complex terrain where the incoming wind can be inherently heterogeneous. Systematically quantifying the effects of different inflows on the present results, which requires a series of additional simulations, will be carried out in the future work.

The present LES study provides useful insights for developing physics-based engineering wake models. In the literature, dynamic wake meandering model [28] is the most commonly used engineering model for predicting the unsteadiness of turbine power output and dynamic loads. Keck *et al.* [52] further developed the dynamic wake meandering model to include the effects of shear on wake deficits and incorporated the turbine-added turbulence for turbine arrays. Hahn *et al.*'s [53] employed a Reynolds-averaged Navier-Stokes (RANS) model to compute the ambient flow in engineering models. Validations of the dynamic wake meandering model can be found in Refs. [29,54,55]. The dynamic wake meandering model assumes that the wake meandering can be modeled as a passive scalar convected by the incoming turbulent flow. However, the LES results in this work showed that the low-frequency, large-scale motion of the wake is dominated by two frequencies, i.e., the low frequency of the inflow, and the frequency of the meandering caused by the wake shear layer instability similar to that of the vortex shedding from bluff bodies [30]. To address this issue, further improvement of the dynamic wake meandering model to account for both the incoming large-scale atmospheric turbulence and the meandering induced by the wake shear layer instability needs to be carried out. In Ref. [56], a physics-based engineering model for wind farms of arbitrary size and layout was developed, which can properly model the interaction of the atmospheric turbulent boundary layer with the turbine wakes. However, it cannot take into account the unsteadiness of the incoming atmospheric turbulence and the turbine wakes. Further development of this kind of engineering model, which does not solve the reduced-order equations as in the dynamic wake meandering model, can also be pursued in the future work by adding a model for the large-scale motion of the wake.

One last note is that whether the coordinated axial induction control is effective or not for maximizing the power production of turbine arrays requires further research as there are many

other factors, such as the ground roughness, turbine spacing, etc., affecting the performance of the control strategy. The present work was devoted to provide insights on the fundamental dynamics of turbine wakes although it is motivated by the coordinated axial induction control.

ACKNOWLEDGMENTS

This work was supported by Xcel Energy through the Renewable Development Fund (Grant No. RD4-13). Computational resources were provided by National Renewable Energy Laboratory, the University of Minnesota Supercomputing Institute, and the Institute for Advanced Computational Science at the Stony Brook University.

APPENDIX: ON THE CALCULATION OF THE POWER SPECTRAL DENSITY (PSD)

Welch's method [49] is employed for the calculation of the PSD. Let $X(j)$, $j = 0, ..., N-1$ be the temporal sequence obtained from LES. To compute the PSD, we first divide $X(j)$ into K

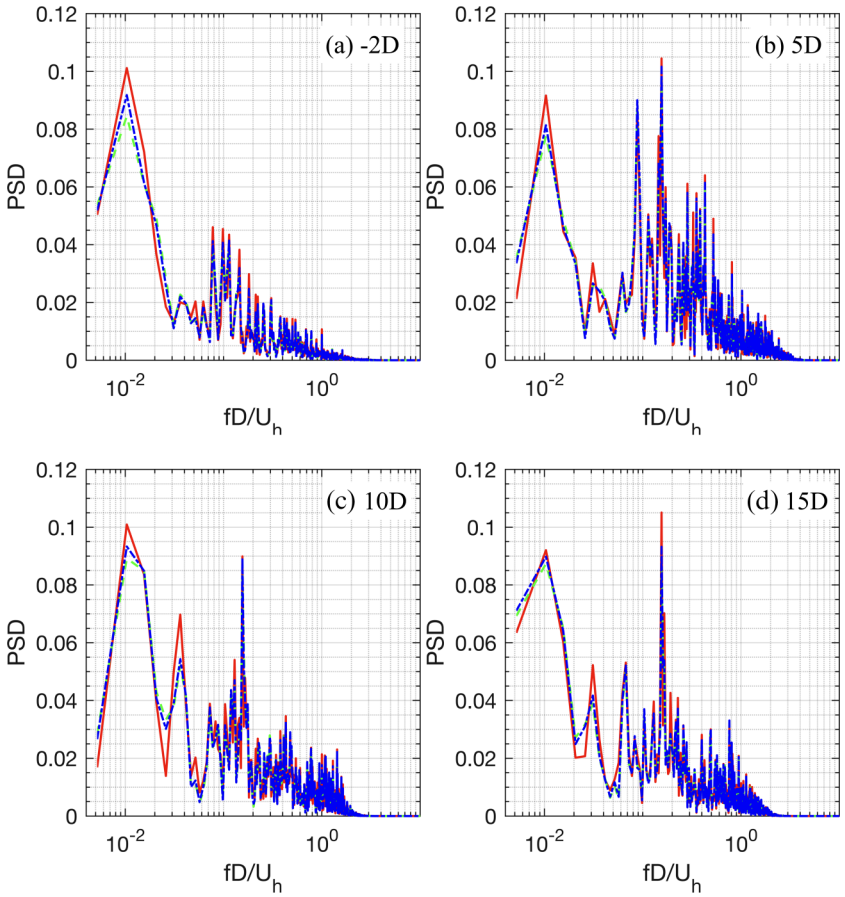

FIG. 17. Effects of different window functions on the PSD profiles at different downwind locations for the $\lambda = 7.8$ case. The PSD is computed using the spanwise velocity fluctuations at different turbine downwind locations along the rotor centerline and normalized by the variance at $x = -2D$. Red solid line, no window function; Green dashed line, W_1; Blue dash-dot line, W_2. The separation between two adjacent segments $S = 20000$.

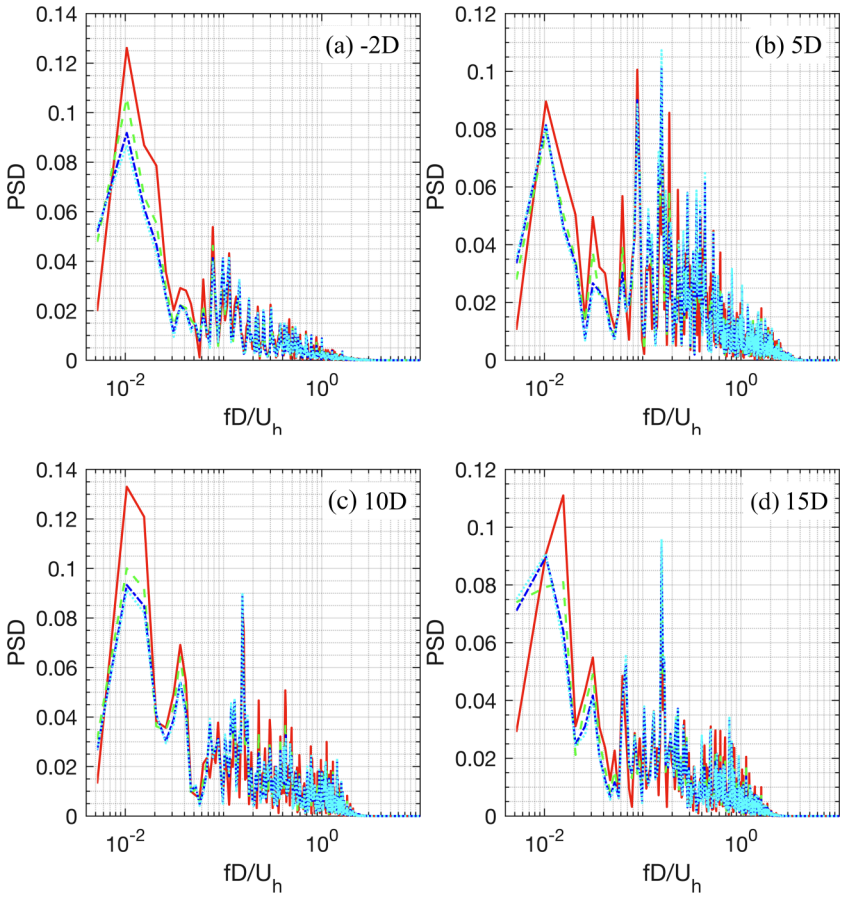

FIG. 18. Effects of different values of separation S on the PSD profiles at different downwind locations for the $\lambda = 7.8$ case. The PSD is computed using the spanwise velocity fluctuations at different turbine downwind locations along the rotor centerline and normalized by the variance at $x = -2D$. Red solid line, $S = 100\,000$; Green dashed line, $S = 50\,000$; Blue dash-dot line, $S = 20\,000$; Cyan dotted line, $S = 10\,000$. We use $L = 100\,000$ and the window function W_2 for tests with different values of S.

segments of length L, so that

$$X_k(j) = X[j + (k-1)S], \quad j = 0, ..., L-1 \tag{A1}$$

are the data items in the kth segment, where $k = 0, ..., K-1$, and S is the separation between two adjacent segments. If the K segments cover the entire sequence, then we have $(K-1)S + L = N$ (from which, we can compute K given S, L, and N). We then perform the discrete Fourier transform on the data items in each segment,

$$A_k(n) = \frac{1}{L}\sum_{j=0}^{L-1} X_k(j)W(j)e^{-i2\pi jn/L}, \tag{A2}$$

where $i = \sqrt{-1}$ for each segment, $W(j)$ is a window function. Two window functions were suggested in Ref. [49], which are as follows:

$$W_1(j) = 1 - \left|\frac{j - \frac{L-1}{2}}{\frac{L+1}{2}}\right|, \quad j = 0, ..., L-1, \tag{A3}$$

and

$$W_2(j) = 1 - \left(\frac{j - \frac{L-1}{2}}{\frac{L+1}{2}} \right)^2, \quad j = 0, ..., L-1. \tag{A4}$$

We finally compute the PSD(f_n) by

$$\mathrm{PSD}(f_n) = \frac{1}{K} \sum_{k=1}^{K} I_k(f_n), \tag{A5}$$

where $f_n = n/L$ (where $n = 0, ..., L/2$), and $I_k(f_n) = \frac{L}{U} |A_k(n)|^2$ [where $k = 1, ..., K$, where $U = \frac{1}{L} \sum_{j=0}^{L-1} W^2(j)$].

In this Appendix, we examine the effects of different window functions and different separations (S) on the computed PSD. For the present simulation, the number of data points of the entire sequence is $N = 200\,000$. In all the tests with different window functions and S, L is fixed at $L = 100\,000$. Figure 17 shows the effects of different window functions on the PSD profiles computed at different turbine downwind locations. As seen the differences between the cases with different window functions are very small especially between W_1 and W_2. We examine the effects of different values of separation S on the PSD calculations in Fig. 18. Four different values of S, i.e., $S = 100\,000$, 50 000, 20 000, and 10 000, are tested, which correspond to $K = 2$, 3, 6, and 11, respectively. Differences between the PSD profiles from $S = 100\,000$ and 50 000 and those from the other two values of S are observed, while the differences between the PSD profiles from $S = 20\,000$ and $S = 10\,000$ are minor.

[1] J. P. Goit and J. Meyers, Optimal control of energy extraction in wind-farm boundary layers, J. Fluid Mech. **768**, 5 (2015).

[2] J. Annoni, P. M. O. Gebraad, A. K. Scholbrock, P. A. Fleming, and J.-W. van Wingerden, Analysis of axial-induction-based wind plant control using an engineering and a high-order wind plant model, Wind Energy **19**, 1135 (2016).

[3] W. Munters and J. Meyers, Dynamic strategies for yaw and induction control of wind farms based on large-eddy simulation and optimization, Energies **11**, 177 (2018).

[4] P. A. Fleming, P. M. O. Gebraad, S. Lee, J.-W. van Wingerden, K. Johnson, M. Churchfield, J. Michalakes, P. Spalart, and P. Moriarty, Evaluating techniques for redirecting turbine wakes using sowfa, Renew. Energy **70**, 211 (2014).

[5] N. Troldborg, J. N. Sorensen, and R. Mikkelsen, Numerical simulations of wake characteristics of a wind turbine in uniform inflow, Wind Energy **13**, 86 (2010).

[6] W. Tian and H. Hu, Effect of oncoming flow turbulence on the kinetic energy transport in the flow around a model wind turbine, in *Proceedings of the 2018 Wind Energy Symposium* (AIAA, 2018), AIAA 2018-0751.

[7] L. P. Chamorro and F. Porté-Agel, A wind-tunnel investigation of wind-turbine wakes: Boundary-layer turbulence effects, Bound.-Layer Meteorol. **132**, 129 (2009).

[8] L. P. Chamorro and F. Porté-Agel, Effects of thermal stability and incoming boundary-layer flow characteristics on wind-turbine wakes: A wind-tunnel study, Bound.-Layer Meteorol. **136**, 515 (2010).

[9] W. Zhang, C. D. Markfort, and F. Porté-Agel, Wind-turbine wakes in a convective boundary layer: A wind-tunnel study, Bound.-Layer Meteorol. **146**, 161 (2013).

[10] K. B. Howard, J. S. Hu, L. P. Chamorro, and M. Guala, Characterizing the response of a wind turbine model under complex inflow conditions, Wind Energy **18**, 729 (2015).

[11] L. P. Chamorro, C. Hill, V. S. Neary, B. Gunawan, R. E. A. Arndt, and F. Sotiropoulos, Effects of energetic coherent motions on the power and wake of an axial-flow turbine, Phys. Fluids **27**, 055104 (2015).

[12] M. M. Hand, N. D. Kelley, and M. J. Balas, Identification of wind turbine response to turbulent inflow structures, in *Proceedings of the ASME/JSME 2003 4th Joint Fluids Summer Engineering Conference* (American Society of Mechanical Engineers, New York, 2003), p. 2557.
[13] F. Bingöl, J. Mann, and G. C. Larsen, Light detection and ranging measurements of wake dynamics, part I: One-dimensional scanning, Wind energy **13**, 51 (2010).
[14] J.-J. Trujillo, F. Bingöl, G. C. Larsen, J. Mann, and M. Kühn, Light detection and ranging measurements of wake dynamics, part II: Two-dimensional scanning, Wind Energy **14**, 61 (2011).
[15] S. El-Asha, L. Zhan, and G. V. Iungo, Quantification of power losses due to wind turbine wake interactions through scada, meteorological, and wind lidar data, Wind Energy **20**, 1823 (2017).
[16] X. Yang, F. Sotiropoulos, R. J. Conzemius, J. N. Wachtler, and M. B. Strong, Large-eddy simulation of turbulent flow past wind turbines/farms: The Virtual Wind Simulator (VWiS), Wind Energy **18**, 2025 (2015).
[17] D. Foti, X. Yang, F. Campagnolo, D. Maniaci, and F. Sotiropoulos, On the use of spires for generating inflow conditions with energetic coherent structures in large eddy simulation, J. Turb. **18**, 611 (2017).
[18] F. Viola, G. V. Iungo, S. Camarri, F. Porté-Agel, and F. Gallaire, Prediction of the hub vortex instability in a wind turbine wake: Stability analysis with eddy-viscosity models calibrated on wind tunnel data, J. Fluid Mech. **750**, R1 (2014).
[19] K. B. Howard, A. Singh, F. Sotiropoulos, and M. Guala, On the statistics of wind turbine wake meandering: An experimental investigation, Phys. Fluids **27**, 075103 (2015).
[20] L. A. Martínez Tossas, R. J. A. M. Stevens, and C. Meneveau, Wind turbine large-eddy simulations on very coarse grid resolutions using an actuator line model, in *Proceedings of the 34th Wind Energy Symposium* (AIAA, 2016), AIAA 2016-1261.
[21] D. Foti, X. Yang, M. Guala, and F. Sotiropoulos, Wake meandering statistics of a model wind turbine: Insights gained by large eddy simulations, Phys. Rev. Fluids **1**, 044407 (2016).
[22] S. Kang, X. Yang, and F. Sotiropoulos, On the onset of wake meandering for an axial flow turbine in a turbulent open channel flow, J. Fluid Mech. **744**, 376 (2014).
[23] C. Santoni, K. Carrasquillo, I. Arenas-Navarro, and S. Leonardi, Effect of tower and nacelle on the flow past a wind turbine, Wind Energy **20**, 1927 (2017).
[24] C. Santoni, U. Ciri, M. Rotea, and S. Leonardi, Development of a high-fidelity CFD code for wind farm control, in *Proceedings of the American Control Conference (ACC'15)* (IEEE, Chicago, IL, 2015), pp. 1715–1720.
[25] X. Yang and F. Sotiropoulos, A new class of actuator surface models for wind turbines, Wind Energy **21**, 285 (2018).
[26] X. Yang, K. B. Howard, M. Guala, and F. Sotiropoulos, Effects of a three-dimensional hill on the wake characteristics of a model wind turbine, Phys. Fluids **27**, 025103 (2015).
[27] D. Foti, X. Yang, and F. Sotiropoulos, Similarity of wake meandering for different wind turbine designs for different scales, J. Fluid Mech. **842**, 5 (2018).
[28] G. C. Larsen, H. A. Madsen, F. Bingöl, J. Mann, S. Ott, J. N. Sørensen, V. Okulov, N. Troldborg, M. Nielsen, K. Thomsen *et al.*, *Dynamic wake meandering modeling* (Risø National Laboratory, Technical University of Denmark, Roskilde, Denmark, Risø, 2007).
[29] T. J. Larsen, H. A. Madsen, G. C. Larsen, and K. S. Hansen, Validation of the dynamic wake meander model for loads and power production in the Egmond aan Zee wind farm, Wind Energy **16**, 605 (2013).
[30] D. Medici and P. H. Alfredsson, Measurements on a wind turbine wake: 3D effects and bluff body vortex shedding, Wind Energy **9**, 219 (2006).
[31] D. Medici and P. H. Alfredsson, Measurements behind model wind turbines: Further evidence of wake meandering, Wind Energy **11**, 211 (2008).
[32] D. Foti, X. Yang, F. Campagnolo, D. Maniaci, and F. Sotiropolos, On the wake meandering of a model wind turbine operating in two different regimes, Phys. Rev. Fluids **3**, 054607 (2018).
[33] A. Calderer, X. Yang, D. Angelidis, A. Khosronejad, T. Le, S. Kang, A. Gilmanov, L. Ge, and I. Borazjani, *Virtual Flow Simulator*, Tech. Rep. (University of Minnesota, 2015).

[34] A. Calderer, X. Guo, L. Shen, and F. Sotiropoulos, Fluid–structure interaction simulation of floating structures interacting with complex, large-scale ocean waves and atmospheric turbulence with application to floating offshore wind turbines, J. Comput. Phys. **355**, 144 (2018).
[35] X. Yang, M. Pakula, and F. Sotiropoulos, Large-eddy simulation of a utility-scale wind farm in complex terrain, Appl. Energy **229**, 767 (2018).
[36] M. Germano, U. Piomelli, P. Moin, and W. H. Cabot, A dynamic subgrid-scale eddy viscosity model, Phys. Fluids A: Fluid Dynam. **3**, 1760 (1991).
[37] L. Ge and F. Sotiropoulos, A numerical method for solving the 3D unsteady incompressible Navier–Stokes equations in curvilinear domains with complex immersed boundaries, J. Comput. Phys. **225**, 1782 (2007).
[38] X. Yang, X. Zhang, Z. Li, and G.-W. He, A smoothing technique for discrete delta functions with application to immersed boundary method in moving boundary simulations, J. Comput. Phys. **228**, 7821 (2009).
[39] Z. Du and M. S. Selig, A 3D stall-delay model for horizontal axis wind turbine performance prediction, in *Proceedings of ASME Wind Energy Symposium, Aerospace Sciences Meetings* (AIAA, 1998), AIAA-98-0021.
[40] W. Z. Shen, J. N. Sørensen, and R. Mikkelsen, Tip loss correction for actuator/Navier–Stokes computations, J. Sol. Energy Eng. **127**, 209 (2005).
[41] Wen Zhong Shen, R. Mikkelsen, J. N. Sørensen, and C. Bak, Tip loss corrections for wind turbine computations, Wind Energy **8**, 457 (2005).
[42] H. Schlichting and K. Gersten, *Boundary-layer Theory* (Springer Science & Business Media, Berlin, 2003).
[43] J. Hong, M. Toloui, L. P. Chamorro, M. Guala, K. Howard, S. Riley, J. Tucker, and F. Sotiropoulos, Natural snowfall reveals large-scale flow structures in the wake of a 2.5-mw wind turbine, Nat. Commun. **5**, 4216 (2014).
[44] L. P. Chamorro, S.-J. Lee, D. Olsen, C. Milliren, J. Marr, R. E. A. Arndt, and F. Sotiropoulos, Turbulence effects on a full-scale 2.5 mw horizontal-axis wind turbine under neutrally stratified conditions, Wind Energy **18**, 339 (2015).
[45] K. B. Howard and M. Guala, Upwind preview to a horizontal axis wind turbine: A wind tunnel and field-scale study, Wind Energy **19**, 1371 (2016).
[46] X. Yang, J. Annoni, P. Seiler, and F. Sotiropoulos, Modeling the effect of control on the wake of a utility-scale turbine via large-eddy simulation, in *Proceedings of the Journal of Physics: Conference Series*, Vol. 524 (IOP Publishing, Bristol, UK, 2014), p. 012180.
[47] X. Yang, J. Hong, M. Barone, and F. Sotiropoulos, Coherent dynamics in the rotor tip shear layer of utility-scale wind turbines, J. Fluid Mech. **804**, 90 (2016).
[48] D. Yang, C. Meneveau, and L. Shen, Effect of downwind swells on offshore wind energy harvesting—A large-eddy simulation study, Renew. Energy **70**, 11 (2014).
[49] P. Welch, The use of fast fourier transform for the estimation of power spectra: A method based on time averaging over short, modified periodograms, IEEE Trans. Audio Electroacoust. **15**, 70 (1967).
[50] E. Machefaux, G. C. Larsen, and J. Mann, *Multiple Turbine Wakes* (DTU Wind Energy, Denmark, 2015).
[51] M. Heisel, J. Hong, and M. Guala, The spectral signature of wind turbine wake meandering: A wind tunnel and field-scale study, Wind Energy **21**, 715 (2018).
[52] R.-E. Keck, M. de Maré, M. J. Churchfield, S. Lee, G. Larsen, and H. A. Madsen, Two improvements to the dynamic wake meandering model: Including the effects of atmospheric shear on wake turbulence and incorporating turbulence build-up in a row of wind turbines, Wind Energy **18**, 111 (2015).
[53] S. Hahn, E. Machefaux, Y. Hristov, M. Albano, and R. Threadgill, Estimation of annual energy production using dynamic wake meandering in combination with ambient CFD solutions, in *Proceedings of the Journal of Physics: Conference Series*, Vol. 753 (IOP Publishing, Bristol UK, 2016), p. 032043.
[54] M. J. Churchfield, S. Lee, P. J. Moriarty, Y. Hao, M. A. Lackner, R. Barthelmie, J. K. Lundquist, and G. Oxley, A comparison of the dynamic wake meandering model, large-eddy simulation, and field data at the Egmond aan Zee offshore wind plant, in *Proceedings of the 33rd Wind Energy Symposium* (AIAA, 2015), AIAA 2015-0724.

[55] T. J. Larsen, G. C. Larsen, M. M. Pedersen, K. Enevoldsen, and H. A. Madsen, Validation of the dynamic wake meander model with focus on tower loads, in *Proceedings of the Journal of Physics: Conference Series*, Vol. 854 (IOP Publishing, Bristol, UK, 2017), p. 012027.

[56] X. Yang and F. Sotiropoulos, Analytical model for predicting the performance of arbitrary size and layout wind farms, Wind Energy **19**, 1239 (2016).